Laurenz Nothdurfter, BSc

LAESIO - Biomechanical Investigation of Coronary Arteries to Stenting and Microstructural Analysis using Multiphoton Microscopy Imaging

MASTER'S THESIS

to achieve the university degree of

Diplom-Ingenieur

Master's degree programme: Biomedical Engineering

submitted to

Graz University of Technology

Supervisor

Prof. Gerhard A. Holzapfel, PhD

Co-Supervisor

Markus A. Geith, M.Sc

Institute of Biomechanics

Graz, May 2020

Affidavit

I declare that I have authored this thesis independently, that I have not used other than the declared sources/resources, and that I have explicitly indicated all material which has been quoted either literally or by content from the sources used. The text document uploaded to TUGRAZonline is identical to the present master's thesis dissertation.

_____
date

_____
signature

Contents

Abstract

In 2017, $92.13\,\%$ of all percutaneous coronary intervention cases in Austria were treated with a stent [1]. Unfortunately, it comes to vascular trauma during the stent implantation. In this thesis a working test protocol was found and biomechanical experiments are conducted, in which the mechanical softening of the tissue under physiological loading conditions of a stent indentation is simulated *in vitro*. Until now, to the knowledge of the author the mechanical response of arteries to stenting is not yet quantified. This Thesis is a part of the FWF funded *LAESIO* project, which has the overall objective to develop a mechanobiological material damage model to mathematically describe the damage mechanisms inside the arterial wall due to stenting. The results of this thesis are prerequisites to develop such a damage model for stent optimization. Such model is intended to be used by scientists and stent manufacturers through implementation into finite element analyses software packages to optimize stents and stent delivery systems by limiting damage to the coronary artery during stent intervention.

To quantify the mechanical behavior of porcine coronary arteries under physiological load the LAESIO testing device [2] was used, which simulates the contact force between a stent strut and the arterial wall. Inside a testing chamber, a square sample of a porcine coronary artery was physiologically stretched in two orthogonal directions, while a stamp in the shape of a stent-strut was indented into the sample. Further, the tested samples were investigated using two different imaging techniques to define the damage mechanisms occurred due to the stent indentation, i.e. by light microscopy and second-harmonic generation imaging.

With the LAESIO testing device and the working test protocol biomechanical experiments were performed successfully. The mechanical response of porcine coronary arteries showed slightly viscoelastic and nonlinear behavior. The tissue could be loaded to the physiological and supraphysiological loads without rupture, but showed severe softening due to the stamp indentation. Damage mechanisms could be identified during the second-harmonic generation imaging. The severity of the damage mechanisms depend on the stamp orientation, i.e. the indentation angle, the used indentation force and the distance between a specific point of interest and the center of the lesion.

Zusammenfassung

Im Jahr 2017 wurden 92,13 % aller perkutanen Koronarinterventionsfälle in Österreich mit einem Stent behandelt [1]. Unglücklicherweise kommt es dabei zu Gefäßverletzungen. Um diese Schädigungen zu minimieren, wird eine gezielte Untersuchung des betroffenen Gewebes benötigt, um die morphologischen und mechanischen Veränderungen durch die Implantation des Stents nachvollziehen zu können. Im Zuge dieser Arbeit wurden biomechanische *in vitro* Experimente durchgeführt und ein Protokoll zum Testen von Koronararterien entwickelt. Die Arbeit wurde im Rahmen des FWF-Projekts *LAESIO* verfasst, welches das übergeordnete Ziel hat, ein mechanobiologisches Materialschädigungsmodell zu entwickeln. Die Ergebnisse dieser Arbeit sind eine wichtige Grundlage für die Entwicklung eines solchen Modells, das die durch den Stent verursachten Schädigungsmechanismen innerhalb der Arterienwand mathematisch beschreiben und in weiterer Folge zur Optimierung von Stents und Stent-Delivery-Systemen dienen soll.

Um eine Quantifizierung der mechanischen Beanspruchung des Gewebes unter physiologischer Belastung zu ermöglichen, wurde das experimentelle Testgerät LAESIO [2] verwendet, mit dem die Kräfte zwischen einer Stentverstrebung und der Arterienwand simuliert werden. Dafür wurde eine quadratische Probe einer Koronararterie vom Schwein physiologisch in zwei orthogonale Richtungen gedehnt, während ein Stempel in Form einer Stent-Verstrebung in die Probe eingedrückt wurde. Anschließend wurden die beschädigten Proben mit zwei verschiedenen bildgebenden Verfahren (Lichtmikroskopie und Frequenzverdoppelung) untersucht, um die aufgetretenen Schädigungsmechanismen definieren zu können.

Mit dem LAESIO Testgerät und dem zugehörigen entwickelten Testprotokoll wurden erfolgreich biomechanische Experimente durchgeführt. Die mechanische Reaktion der Koronararterien zeigte ein leicht viskoelastisches und nichtlineares Verhalten. Das Gewebe konnte den physiologischen und supraphysiologischen Belastungen ausgesetzt werden, ohne zu reißen, wies aber eine starke Erweichung aufgrund des eingedrückten Stempels auf. Mit Hilfe der bildgebenden Verfahren konnten Schädigungsmechanismen identifiziert werden. Diese hängen von der Orientierung des Stempels ab, d.h. vom Eindringwinkel, von der verwendeten Eindringkraft und vom Abstand zwischen einem bestimmten Punkt und dem Zentrum der Läsion.

Acknowledgment

1 Introduction

1.1 Coronary Arteries

As a permanently active pumping organ, the heart has a high oxygen demand. It is covered by the blood supply from the heart's own vessels, called coronary arteries. They originate from small dilations in the ascending aorta, the so-called aortic sinuses, just above the aortic valve. Two main coronary arteries, the left coronary artery (LCA) and the right coronary artery (RCA), supply the left and the right ventricle with oxygen-rich blood, respectively [3].

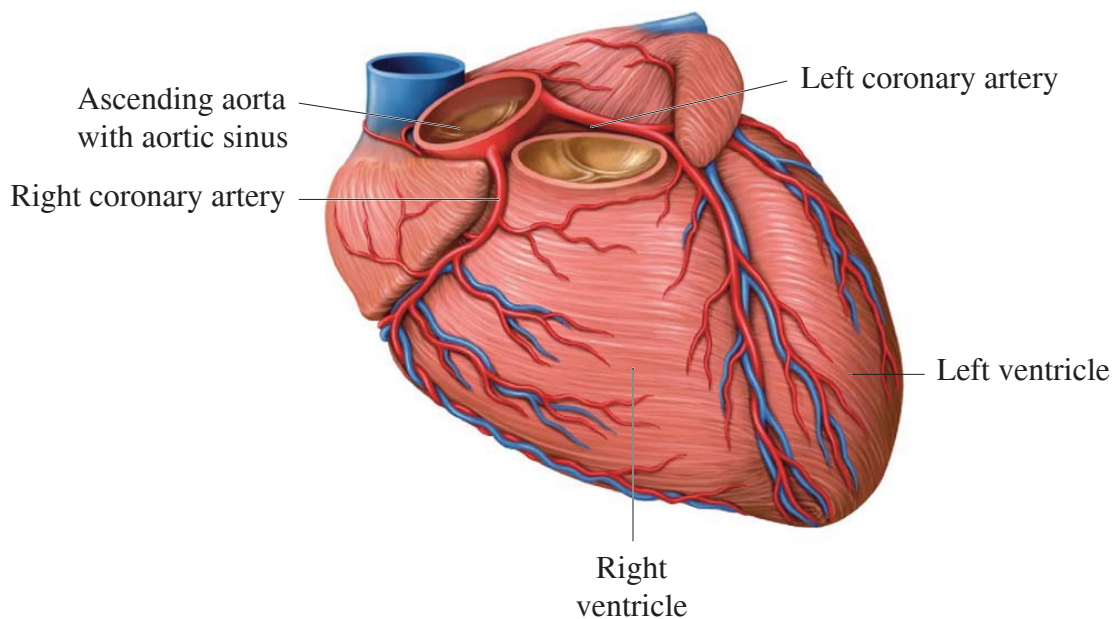Figure 1.1   Heart with coronary arteries, adapted from [3].

Coronary heart disease is the deficiency of blood supply to the myocardium because of a restricted blood flow in the coronary arteries. The main cause are calcifications of the blood vessels, the so-called atherosclerosis, in particular in their proximal parts. The death of the myocardial cells begins when the blood flow falls below 25% of the standard [4].

An artery is composed of three distinct layers, the intima, the media, and the adventitia [5]. Each of these layers has different functions, microstructures, and biomechanical responses. The intima, the innermost layer, comprises a single layer of endothelial cells lining the arterial wall and a subendothelial layer. In young individuals, this layer is almost none existing, but the thickness varies with topography, age and disease. The middle layer, called media, includes a complex network of collagen fibers, elastin fibers, and smooth muscle cells. The fibers in the media are mainly oriented in the circumferential direction, displayed in Figure 1.2. This structured arrangement gives the media the ability to resist high loads in the circumferential direction [6]. The adventitia, the outermost layer, consists of thick bundles of collagen fibers, forming a fibrous tissue. In a physiological state the fibers are in a wavy configuration and are arranged in a helical structure to reinforce the arterial wall. Under higher load the fibers are straightened out to prevent the artery from overstretching and rupture.
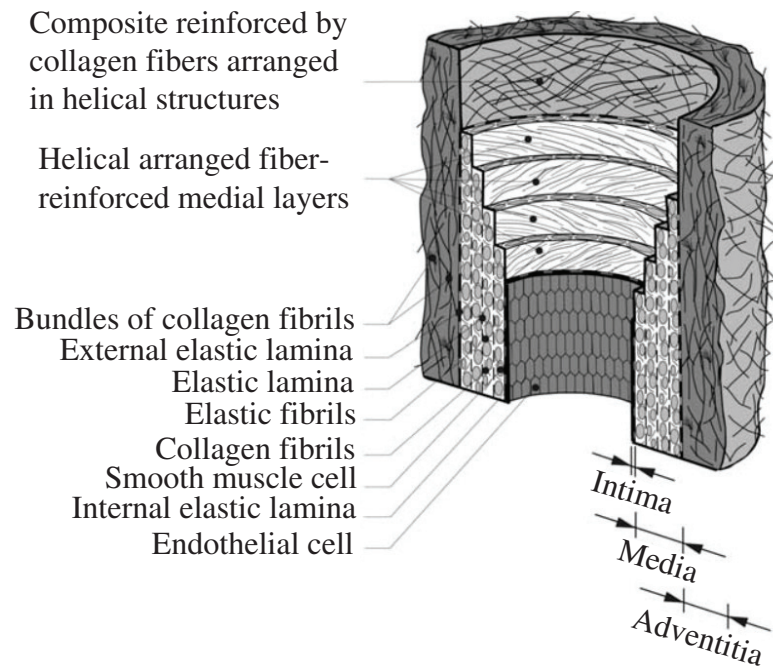
Figure 1.2   Schematic representation of an artery composed of three layers: intima, media, adventitia. Adapted from [5].

Holzapfel et al. [5] describe that in *ex vivo* conditions the mechanical properties are altered due to biological degradation. Therefore, arteries should be tested in appropriate oxygenated, tempered salt solution, as fresh as possible. Arteries show a viscoelastic, nonlinear, and anisotropic mechanical behavior.

Chen and Kassab [7] found that the wall of coronary arteries is composed of the distinct layers, but the fiber orientation changes to the structure described in [6]. The study [7] declares, that the media consists of collagen fibers oriented towards the circumferential direction. The adventitia instead is split up in two parts: the inner adventitia comprises concentric oriented densely packed collagen fiber sheets and the outer adventitia contains collagen fiber bundles oriented towards the longitudinal direction. Towards the exterior of the adventitia the collagen fibers become thicker and are distributed randomly.
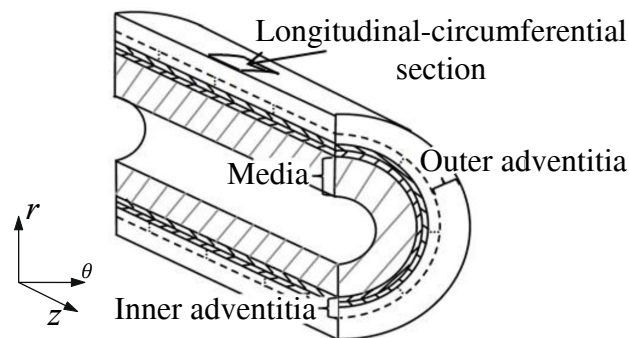

Figure 1.3   Schematic representation of the wall layers of a coronary artery, adapted from [7].

1.2 Percutaneous Coronary Intervention, Vascular Injuries and Restenosis

Percutaneous coronary intervention (PCI) has become one of the most frequently performed therapeutic procedures in medicine. Especially coronary stent intervention (CSI) is used in 70 % of all PCI cases [3]. In Austria, the number of PCI increased by 19 % from 2012 to 2018 with a total amount of 24,462 PCI in the year 2018 [1]. In the past, balloon angioplasty was used, but acute vessel closure limited it. This accelerated the development of stents to maintain lumen integrity [8]. CSI improved the safety during the procedure and narrowed down the number of required surgical procedures [9].

The stent, which is usually crimped on balloon catheters, is positioned in the stenotic coronary section. The balloon gets inflated with a certain internal pressure [10] until the maximum internal balloon pressure, which is specified by the stent manufacturer, is applied and kept constant for a few seconds, overstretching the vessel and the stent. Overstretching is necessary to compensate the stent recoil. The balloon is removed, and the stent remains in the pulsating artery and supports the dilated vessel section so the passageway of the blood is given [3]. Figure 1.4 shows the schematic procedure during CSI.
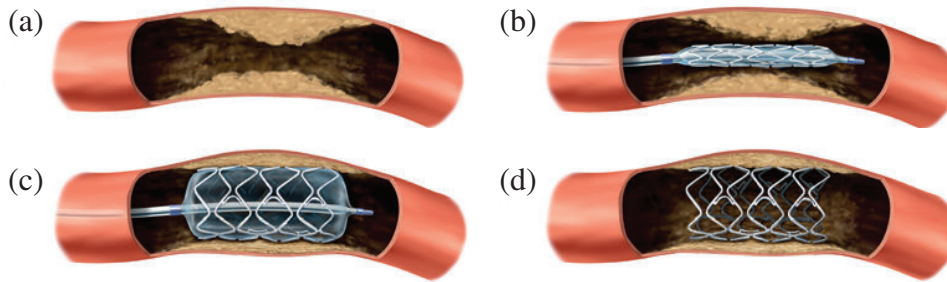
Figure 1.4   Schematic procedure during CSI, adapted from [3]: (a) stenotic coronary
              artery; (b) balloon catheter with non-expanded stent; (c) balloon catheter with
              overexpanded stent; (d) recoiled stent.

During CSI interventions it is unavoidable to not injure the coronary artery which may lead
to neointimal hyperplasia and further to restenosis [11], the most common complication
which occurs in up to 20 % of CSI cases [12]. The severity of vascular injuries is related
to the degree of restenosis. Schwartz et al. [13] were the first to quantify vascular damage
to the stented arteries. They implanted stents in porcine arteries and induced injuries to
the vessel, then they prepared and analyzed histological sections with light microscopes,
and evaluated the lesion with a stent injury score defined in Table 1.1. The thickness of
the neointima is measured, as shown in Figure 1.5(a), with the values a and b for each
wire site. The mean injury score was related to the mean neointimal thickness formed in
the coronary arteries shown in Figure 1.5(b). This states, that the degree of vessel injury
correlates with the thickness of the neointima. In the porcine coronary arteries, sizeable
amounts of the neointima develop identical to that in humans [14]. Schwartz et al. [13]
created a revolutionary tool allowing damage classification of the injury, but the evaluation
of the respective stent injury score is highly subjective. The results could not be correlated
with the load acting on the artery. To inhibit neointimal thickening and restenosis different
types of drug-eluting stents (DES) have emerged, which brings higher risk of late restenosis
and a constant danger of in-stent-thrombosis due to delayed re-endothelialization [12].

Table 1.1   Values for vessel injury score introduced by [13].

Score	Description of injury
0	Internal elastic lamina intact; endothelium typically denuded; media compressed but not lacerated
1	Internal elastic lamina lacerated; media typically compressed but not lacerated
2	Internal elastic lamina lacerated; media visibly lacerated; external elastic lamina intact but compressed
3	External elastic lamina lacerated; typically large lacerations of media extending through the external elastic lamina; coil wires sometimes residing in adventitia

(a)

(b)
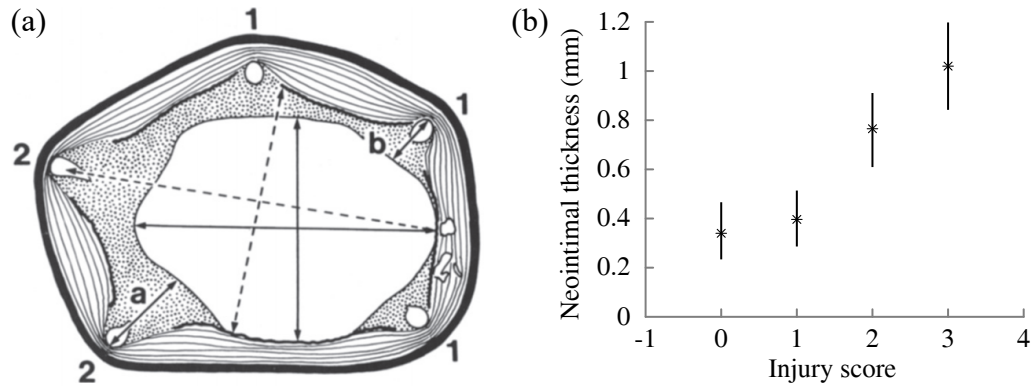
Figure 1.5 (a) Schematic drawing of a vessel showing the measurement of the thickness of the neointima. The dashed lines indicate the major and minor axes of the original lumen while the solid lines indicate the axis of the residual lumen. The injury score of each wire is noted outside of the vessel and a and b are examples how the thickness of the neointima is measured. (b) Neointimal thickness ($\pm$ SD) related to the occurred injury score. Adapted from [13].

Figure 1.6 shows the triaxial loading condition of an artery during the CSI process. The vessel is physiologically stretched by blood pressure so that the tissue experiences tension in the longitudinal and circumferential directions. Additionally, the vessel experiences stent-induced pressure/force in the radial direction, which effects the tension in longitudinal, circumferential and radial direction. A small quadratic sample from a stented coronary artery, shown in Figure 1.6, displays the triaxial loading conditions during CSI on a smaller scale.

Figure 1.6 Triaxial loading conditions during CSI. The artery is exposed to both physiological and stent-induced loadings. Adapted from M. A. Geith, Institute of Biomechanics, Graz University of Technology.

1.3 Biaxial Tensile Testing

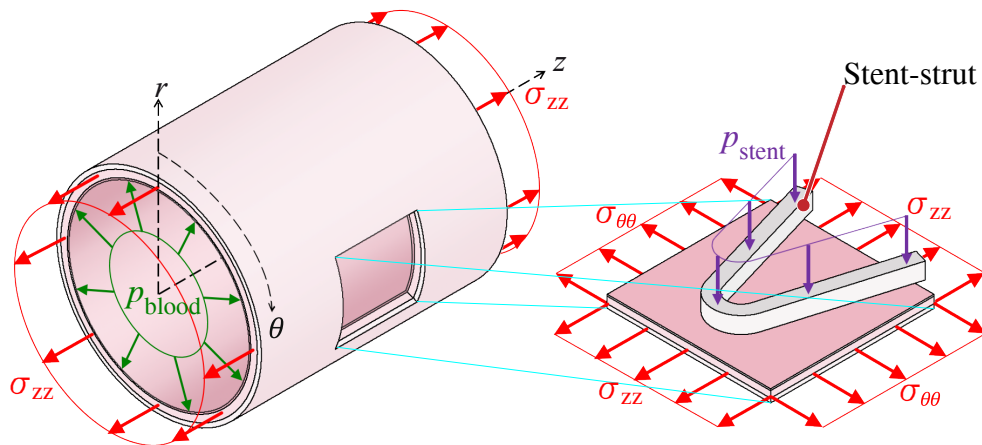The biaxial tensile test is used to investigate the mechanical characterization of soft anisotropic biological tissue. For this, the specimen is immersed in at $37 \pm 1.0\,°C$ tempered phosphate-buffered saline (PBS) bath and biaxially stretched. The temperature and PBS simulate human environmental conditions [15].

The biaxial testing device consists of four linear actuators, which can be controlled independently by force, stretch, or position [16]. On every linear actuator, a load cell measures the force in the longitudinal (z) and circumferential (θ) direction. Figure 1.7 displays that every load cell is connected to a clamping device. The sample is then attached to the clamping device with hooks and threads. The mechanical response of the arterial wall can be determined using biaxial tensile tests. The load is applied to the specimen in two orthogonal directions and its stress strain behavior is measured.

However, the triaxial loading conditions during CSI, shown in Figure 1.6 cannot be mimicked with conventional uni- or planar biaxial tensile tests. Therefore, the LAESIO testing device, presented in Section 2.2, is able to mimic the triaxial loading conditions.
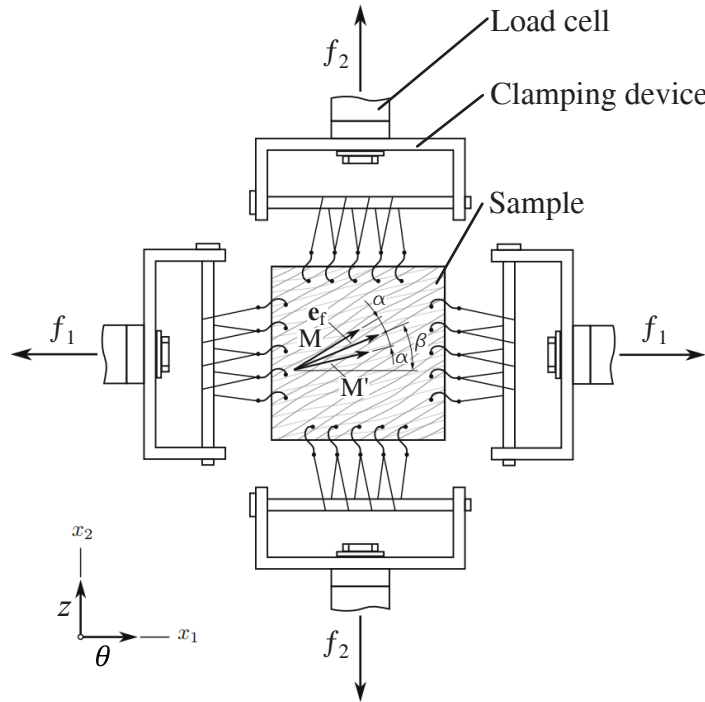
Figure 1.7   Schematic setup of a biaxial tensile testing device adapted from [16]. **M** represents the fiber orientation of the upper layer and **M'** denotes the fiber orientation of the lower layer. The mean fiber direction is described by $\mathbf{e}_f$, where the angle α occurs between $\mathbf{e}_f$ and **M** and $\mathbf{e}_f$ and M'. β describes the in plane orientation of the mean fiber direction in order which corresponds to the angle between the axis θ and $\mathbf{e}_f$. Adapted from [16]

1.4 Second–Harmonic Generation Microscopy

Second-harmonic imaging microscopy (SHIM) is an established microscope imaging contrast mechanism, which is used for visualization of the structure and function of cells and tissue. This is based on the nonlinear optical phenomenon, called second-harmonic generation (SHG). This procedure can take place in a microscope that uses illumination from ultrafast (near-infrared) laser light [17, 18]. SHG is a nearly instantaneous process, in which two photons are converted into a single photon of twice the energy, emitted coherently [17]. There are numerous supramolecular structures within cells and tissues that can produce SHG signals [19], for example, collagen, which is investigated in this thesis.

Because it is a nonlinear process, SHG can be confined to the region of greatest power density at the focus of the microscope, resulting in intrinsic three-dimensional sectioning, without the use of a confocal aperture and reducing out-of-plane photo bleaching and phototoxicity [20].

1.5 Motivation

This Master's Thesis takes place in the framework of the research project *LAESIO - Quantification of Vascular Damage and Cell Proliferation: A Unique Investigation of Stent Implantation* at the Institute of Biomechanics, Graz University of Technology, funded by FWF. The aim of the project is the detection of time- and load-dependent damage mechanisms (DMs) of arterial tissue due to CSI. The project might result in a novel material damage model (MDM), which will describe those mechanisms, their interplay, and their effect on restenosis. The basis for these steps is a deep understanding of the CSI process.

The main focus of this thesis is to gain knowledge of material properties of coronary arteries (CA) and to quantify the mechanical and arterial morphological vascular damage of coronary arteries due to CSI. The mechanical testing was performed on the LAESIO testing device and for the morphological investigation SHG imaging was used. However, the triaxial loading conditions during CSI cannot be mimicked with conventional uni- or planar biaxial tensile tests. Advanced imaging technologies, such as multiphoton microscopy in conjunction with high-frequency SHG lasers allow 3D investigations of collagen fibers, which are shown to be the most relevant components for the strength of arterial tissue. Previous studies have shown [21, 22], that this technology enables the detection of structure-related DMs like changes in the ground matrix or mean collagen fiber direction. Nonetheless, to our knowledge, no work has been published about the SHG investigation of arteries damaged by CSI.

The findings of the *LAESIO* research project will not provide new stent designs or ideas for stent optimization. However, with the unique mechanobiological MDM, it will provide engineers a powerful diagnostic tool to estimate the negative effects of stent prototypes via finite element analyses (FEA) simulations. Above all, the results from LAESIO will help to finally build up urgently needed basic knowledge about CSI injury and restenosis formation from a biomechanical point of view.

1.6 Objectives

CSI is a common used intervention for PCI. Nevertheless, there is a lack of experimental data, describing mechanical and morphological changes of the tissue, due to CSI. Therefore, the goal of this thesis is to measure the mechanical response of porcine coronary arteries, to define DMs in the arterial wall and to describe the underlying patterns of these mechanisms. For the experimental setup the testing device LAESIO was used, which simulates the *in vivo* conditions in an *in vitro* environment. With this testing device coronary arteries have never been tested before. Therefore, an established test protocol for the simulation of a stent indentation needed to be developed. Afterwards, mechanical tests were performed to quantify the mechanical response, using Cauchy stress-stretch diagrams, where the softening of the tissue could be identified. In a next step, the tissue samples were investigated with regard to the morphological changes of the tissue. For this purpose imaging techniques were used, i.e. light microscopy and SHIM. Light microscopy on the one hand, was able to show the structural changes of the tissue in 3D. On the other hand, SHIM made it possible to visualize the microstructural changes of the collagen fibers. Finally, the collected data helped defining DMs in the arterial wall, using structural parameters defined by Holzapfel et al. [22]. This thesis takes place in the framework of the FWF funded project *LAESIO* and can be considered as a foundation for the development of a future MDM, which is the main goal of the project.

2 Material and Method

2.1 Material and Sample Preparation

The target artery for testing is the porcine RCA. Therefore, whole untreated hearts were taken from a local slaughterhouse. The hearts were transported to the laboratory of the Institute of Biomechanics, where the samples were prepared for the tests shown in Figure 2.1(a). The RCA was dissected, with the help of a pair of tweezers and a scalpel, staring from the aortic sinus until the diameter of the RCA was smaller than $4\,\text{mm}$, marked in Figure 2.1(b) with yellow lines. Fat and muscle tissue around the RCA was removed without damaging the target artery. Further, the dissected RCA, presented in Figure 2.1(c), was cut into $15\,\text{mm}$ long tubes, which are shown in Figure 2.1(d). The reaming fat and muscle tissue was removed from the tube, which was then cut open with scissors in the longitudinal direction, marked with the red dotted line in Figure 2.1(d), to get a planar specimen. Finally, a square sample of the RCA with no bifurcations was cut out. The sides needed to be parallel to the longitudinal and circumferential direction. The square samples, shown in Figure 2.1(e), had a size a between 8 and $9.5\,\text{mm}$ for each side and a thickness T_0 between 0.72 and $1.05\,\text{mm}$. The circumferential direction was marked with a tissue marker (*mediware H7 00350; Wesel, Germany*) to distinguish between the longitudinal and circumferential direction for subsequent tests. The length and the amount of samples was varying for every RCA. The difficulty was to find samples without bifurcations. After preparation, the RCA was placed inside a bath of PBS to keep the samples hydrated.

2.1.1 Sample Storing

For storing, the RCA samples were snap-frozen to stop the biological degradation. The protocol was taken and replicated from Čepin [23]. For this process, liquid nitrogen and 2-Methylbutane were required. First, the liquid nitrogen was poured into a dish-shaped Dewar flask (*Dish-shaped Dewar flask, KGW Isotherm; Karlsruhe, Germany*). Second, a glass beaker containing methyl butane (*2-Methylbutane, Carl Roth; Karlsruhe Germany*) was placed in the dish-shaped Dewar flask for precooling. The methyl butane prevented the formation of blisters on the sample and prevented water from crystallizing on the outside of the specimen while freezing, to preserve the structure of the sample [24]. It was essential to wait until the methyl butane formed solid ice at the wall of the glass beaker, which is a sign that the temperature of approximately $-160°\text{C}$ was reached. Third, the sample was placed into the methyl butane with tweezers [23]. Finally, after 60 seconds, the frozen sample was transferred into a labeled container (*C567-Spectainer, Simport Scientific; Canada*)

and stored at $-80°$C. Pretests of defrosted snap-frozen samples showed non-reproducible results. The author assumes that this occurs because of active cell behavior. Therefore, the samples stored at $-80°$C were defrosted in phosphate-buffered saline (PBS) and washed twice with PBS, so there was no remaining methyl butane on the sample. At last, the samples got frozen and stored at $-20°$C in PBS, until they were needed for testing. This method inhibited the activity of the smooth muscle cells (SMC), so the sample had only a passive behavior.
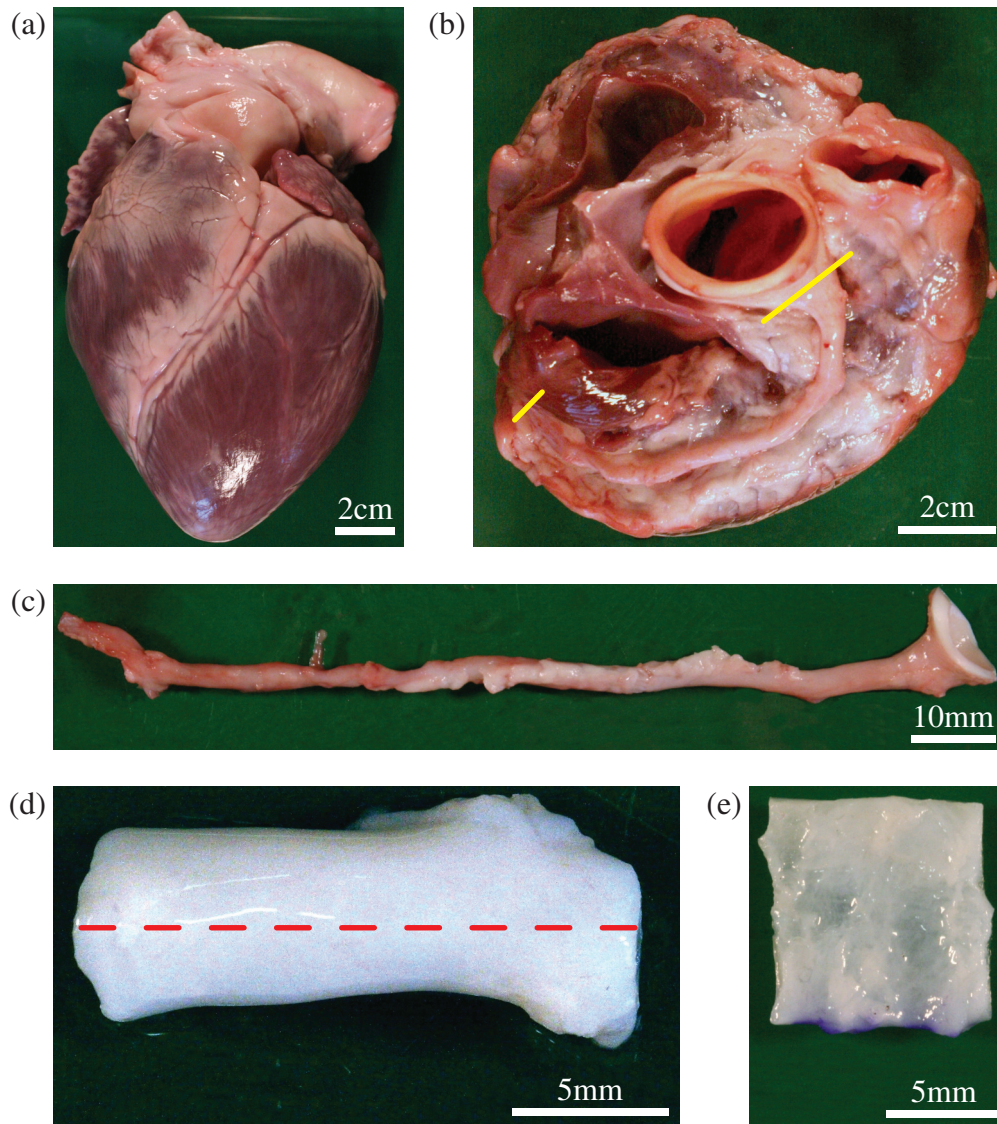

Figure 2.1   Sample preparation: (a) front view of an untreated heart; (b) top view of the heart with half dissected RCA; (c) dissected RCA; (d) 15 mm RCA tube; (e) planar squareed sample.

2.2 Experimental Setup – LAESIO

To quantify the mechanical and morphological vascular damage due to stent indentation a normal biaxial testing device, which is described by Sommer et al. [15] is not suitable. Therefore, the experiments were performed on the LAESIO testing device [2], shown in Figure 2.2(a). This testing device simulates the mechanical loading of an artery sample due to stent indentation. The setup of the LAESIO comprises a force-driven biaxial tensile testing stage to apply planar physiological loads on rectangular specimens of arteries. The triple-axis-unit allows the indentation of a stamp, in the shape of a stent strut, into arterial tissues under a specified loading [2]. Figure 2.2(b) shows the interior of the LAESIO testing device and consists of a specimen bath with a heating coil, which is connected with a heating circulator (*ED (v.2), Julabo; Seelbach, Germany*) to keep the solution in the bath at the specific temperature of 37 ± 1.0°C. The specimen bath has a Luer-Lock with a three-way stopcock at the bottom of the bath, where the solution can be added with the help of an infusomat from an external bottle during the test. Solution needs to be added because it comes to evaporation of the liquid during the experiment. Additionally, an overflow to prevent spillover due to the added solution was installed. The overflow was fixed to one sidewall of the specimen bath and is designed to drain off liquids that are 2 mm below the edge. The setup of the infusomat and the overflow were designed and realized by Heiml [25]. Figure 2.3 shows the schematic LAESIO-testing machine setup. The biaxial tensile testing stage consists of four linear stages (*ST4018M1804-KOWI1, Nanotec Electronic; Feldkirchen, Germany*) with 5 N load cells (*KD40s 5N, ME-Meßsysteme; Hennigsdorf, Germany*) and an accuracy of 0.1 % mounted on top. With this combination physiological stretch, that appears due to blood pressure, is applied to the quadratic sample. The brackets work as a connecting device between the sample and the load cells and are fixed on the load cells with knurled nuts, as shown in Figure 2.5.

The triple-axis-unit, shown in Figure 2.2(b), 2.3 and 2.4, holds a 2 N three-component sensor (*K3D40 2N, ME-Meßsysteme; Hennigsdorf, Germany*), with an accuracy of 0.1 % to set the specified stamp loading. The stamp is mounted on the sensor, with the shape of a modern stent strut with a width of $b = 0.08$ mm [26] and a length of $l = 3$ mm, shown in Figure 2.6. The orientation of the stamp can be varied in every angle in the radial direction. The videoextensometer (VE) is a non-contact 2D video strain measurement technique and comprises a camera (*Model µEye UI-3243-CP-M-GL, IDS; Obersulm, Germany*) and a lens (*23FM75L, Tamaron; Japan*). It is mounted below the biaxial stage and measures the local deformation in the circumferential and longitudinal direction through a window in the bottom of the specimen bath, with an accuracy of ± 0.015 mm. The used software for the VE is *LaserXtens*(*Zwick/Roell; Ulm, Germany*).
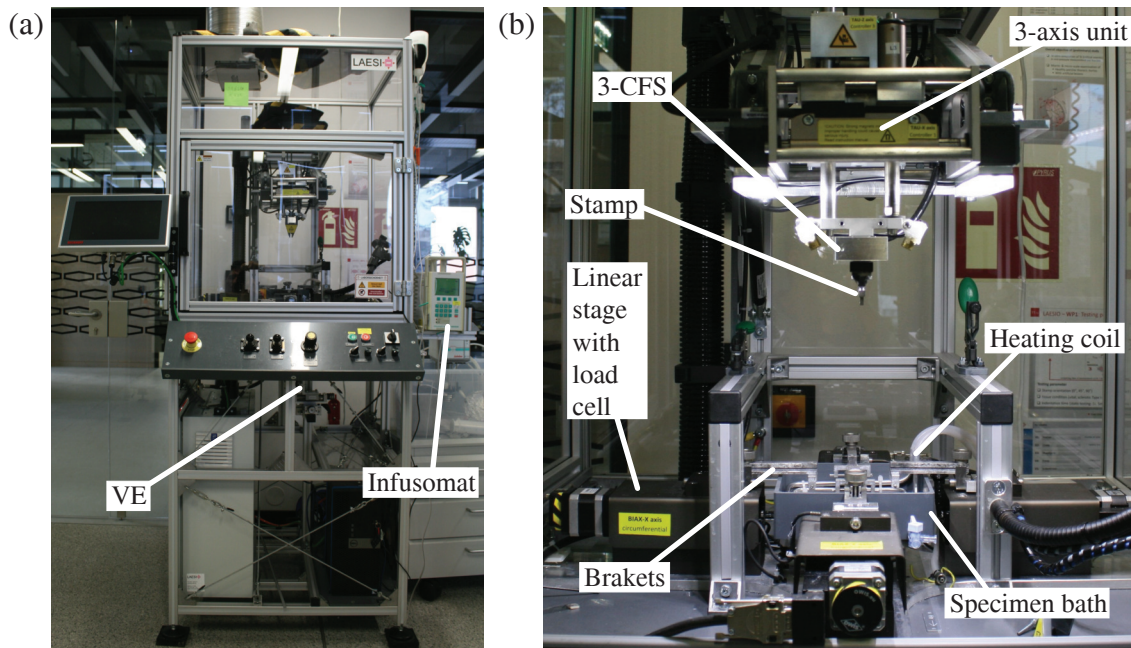
Figure 2.2   (a) LAESIO testing device; (b) interior of the LAESIO testing device.
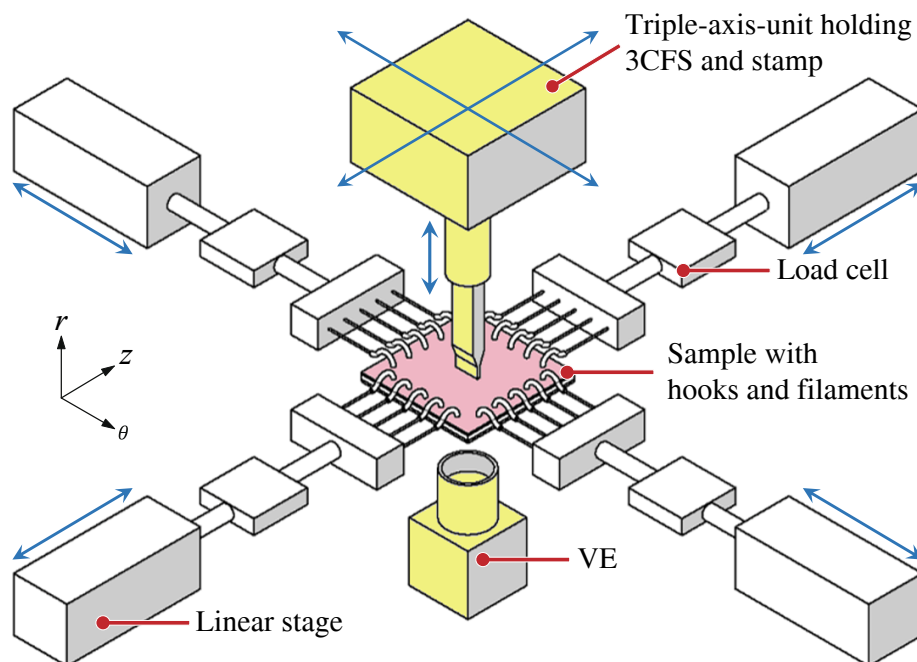
Figure 2.3   Schematic of the LAESIO-testing machine setup. Adapted from M. A. Geith,
             Institute of Biomechanics, Graz University of Technology.

(a)

(b)

3-CFS

3-CFS
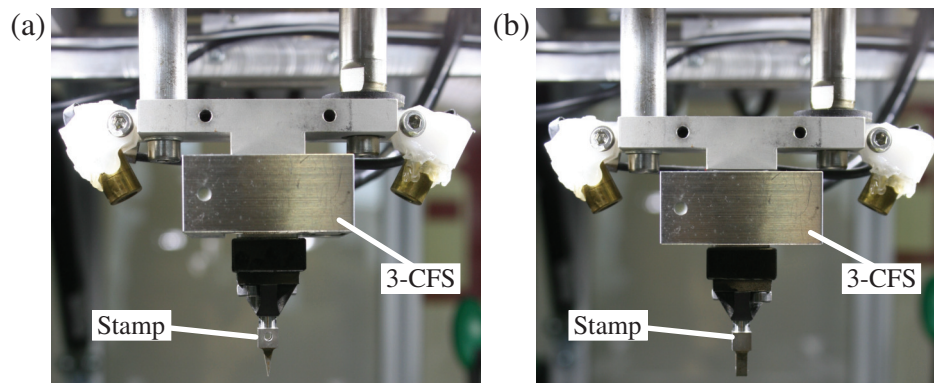
Stamp

Stamp

Figure 2.4   Detailed image of the three-component sensor and the stamp in two possible
             angles: (a) longitudinal stamp orientation; (b) circumferential stamp orienta-
             tion.

Knurled nuts

Load cell

Brackets

Figure 2.5   Detailed image of the linear stage with the load cell mounted on top and the
             brackets fixed with the knurled nuts.

0.08 mm

Figure 2.6   Stent with the dimensions of one strut. Adapted from M. A. Geith, Institute
             of Biomechanics, Graz University of Technology.

2.3 Testing Scenarios and Testing Protocols

Every test was performed in a $37 \pm 1.0°$C tempered PBS bath with a pH-value within the range of 7.35 to 7.45. Therefor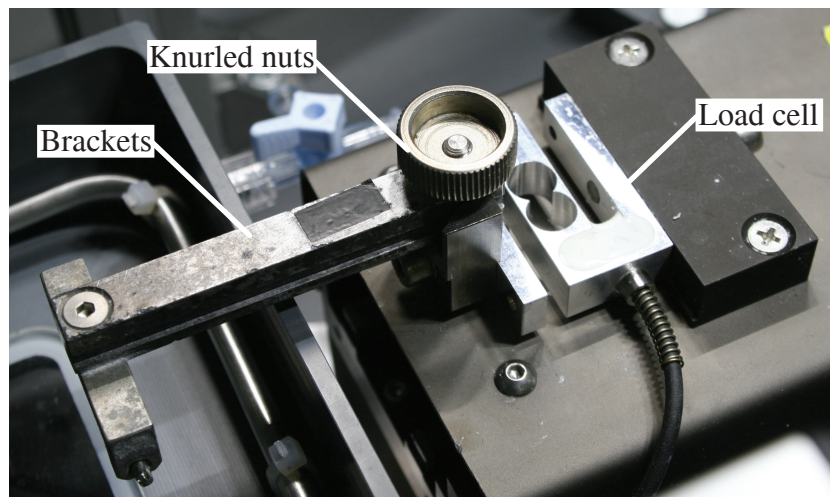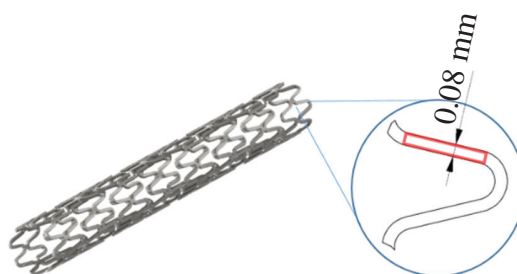e, fresh PBS solution was mixed for every test with a premixed PBS powder (*Roti-PreMix PBS, Carl Roth; Karlsruhe, Germany*). The testing velocity was $v = 1$ mm/min for the biaxial tensile testing stage and the triple-axis-unit. For the calculations of the physiological state of a RCA the internal pressure of 130 mmHg was used. The mean diameter $d = 3.44$ mm and the mean wall thickness $T = 0.74$ mm of the RCA were taken from van Andel et al. [27]. The first Piola-Kirchhoff stress P_{zz} and $P_{\theta\theta}$ for the physiological state was calculated using the formula for thin-walled vessels as follows:

$$P_{zz} = \frac{p\,(D - T)}{4T} \quad \text{and} \quad P_{\theta\theta} = \frac{p\,(D - T)}{2T}, \tag{2.1}$$

where p denotes the RCA internal pressure, d the RCA internal diameter and T the thickness of the RCA. This results in first Piola-Kirchhoff stress of $P_{zz} = 15.9$ kPa in the longitudinal direction and $P_{\theta\theta} = 31.6$ kPa in the circumferential direction. The forces applied to the sample on every side were computed with

$$f_{zz} = |f_{zz}^{+}| = |f_{zz}^{-}| = P_{zz}\, L\, T_0 \quad \text{and} \quad f_{\theta\theta} = |f_{\theta\theta}^{-}| = |f_{\theta\theta}^{-}| = P_{\theta\theta}\, L\, T_0\,, \tag{2.2}$$

in which L is the length of one side of the squared sample, assumed that every edge has the same length. T_0 defines the mean thickness of the sample, which was measured with a VE with an accuracy of ± 0.015 mm. The thickness on every edge of the sample was measured and the mean thickness T_0 was then calculated.

For the sake of simplicity the indentation tests were performed with two stamp orientations. One stamp orientation is parallel to the longitudinal axis defined as angle $\iota = 0°$, shown in Figure 2.7 (a). The other direction is defined as $\iota = 90°$, so the stamp is perpendicular to the longitudinal axis, shown in Figure 2.7 (b). The stamp force was either $F_{\text{ind}} = 1$ N or $F_{\text{ind}} = 2$ N, which results, due to the area 0.24 mm^2 of the stamp, in a pressure of $p_{\text{ind}} = 4.14$ MPa and $p_{\text{ind}} = 8.3$ MPa, respectively.

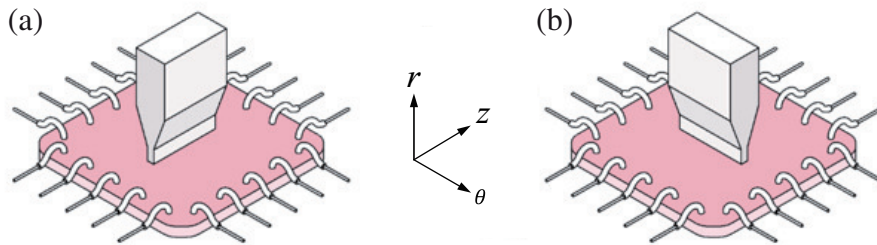

Figure 2.7   Stamp orientation. (a) Stamp indenting at the angle of $\iota = 0°$. (b) Stamp indenting at the angle of $\iota = 90°$. Adapted from M. A. Geith, Institute of Biomechanics, Graz University of Technology

2.3.1 Sample Preparation

First it was necessary to set up connections between the sample and the linear stages of the testing device. Therefore, four fishing hooks (*Patriot Barbless Ideal Dry # 18, Partridge of Redditch, Wincanton, Somerset, UK*) were placed at each side of the square planar sample, as shown in Figure 2.8. This was realized with a pair of tweezers and a cube of foam to place the sample on an elevated position. This helped to place the hooks in a symmetric pattern on every edge. The hooks were attached to a suture (*Terylene USP 5; Serag-Wiessner, Germany*), where the first and the last hook were knotted to the suture. The two hooks in between were strung up on the sutures, so they could move freely. Further, all four sutures deeded to have the same length. This setup should provide similar forces on every hook. The sutures with the hooks were used to connect the sample to the testing device. With four hooks on each edge of the sample, a constant distance between every hook and a similar hook arrangement, a uniform strain distribution should be given. This setup is based on the work of Eilaghi et al. [28], who investigated the strain uniformity with respect of number and location of attachment points. During the hooking process, it was important to keep the sample moistened with PBS.
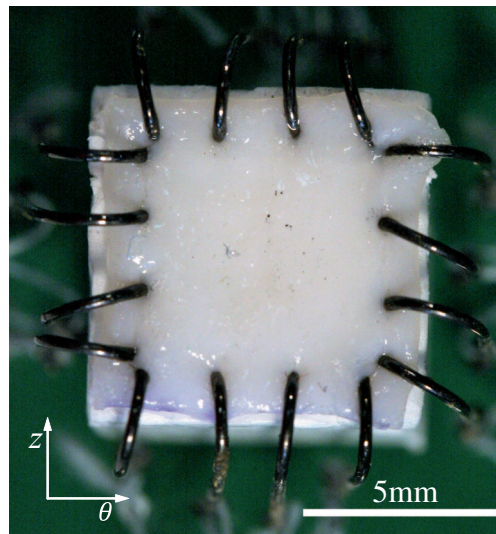
Figure 2.8   Hooked sample, placed on the foam cube. The front side is marked with a
             purple tissue marker which indicates one longitudinal side.

The next step was to place the hooked sample in a holding device, as shown in Figure 2.9, to center it inside the brackets in a trampoline fashion with the adventitia facing upwards. The sample needed to be in the center of the brackets to make sure that the sample is in the center of the testing device. The adventitia was then covered with fine black dots of a special tissue ink (*Tissue marking dyes, black 3408-3, BioGnost; Zagreb, Croatia*), using a fine brush. These dots serve as optical markers and improve the contrast of the sample. This was important for the optical tracking of the local deformation. Figure 2.14 shows

the black dots and the pattern for the optical tracing. Afterwards, the four brackets with the sample were moved via the holding device to the testing machine and mounted to the linear stages via knurled nuts, displayed in Figure 2.5.

Before the test could be started, the sample needed to be preloaded with a force of $0.01\,\text{N}$, to make sure that the sample is on one level and to prevent the sample from sagging. In this state, the sample must be brought into focus. Therefore, the lens was set manually and the VE had to be calibrated. For this purpose, a piece of scale paper is placed underneath the sample and the correct distance is entered in the *LaserXtens* software. Before the test, the load cells were set to zero.

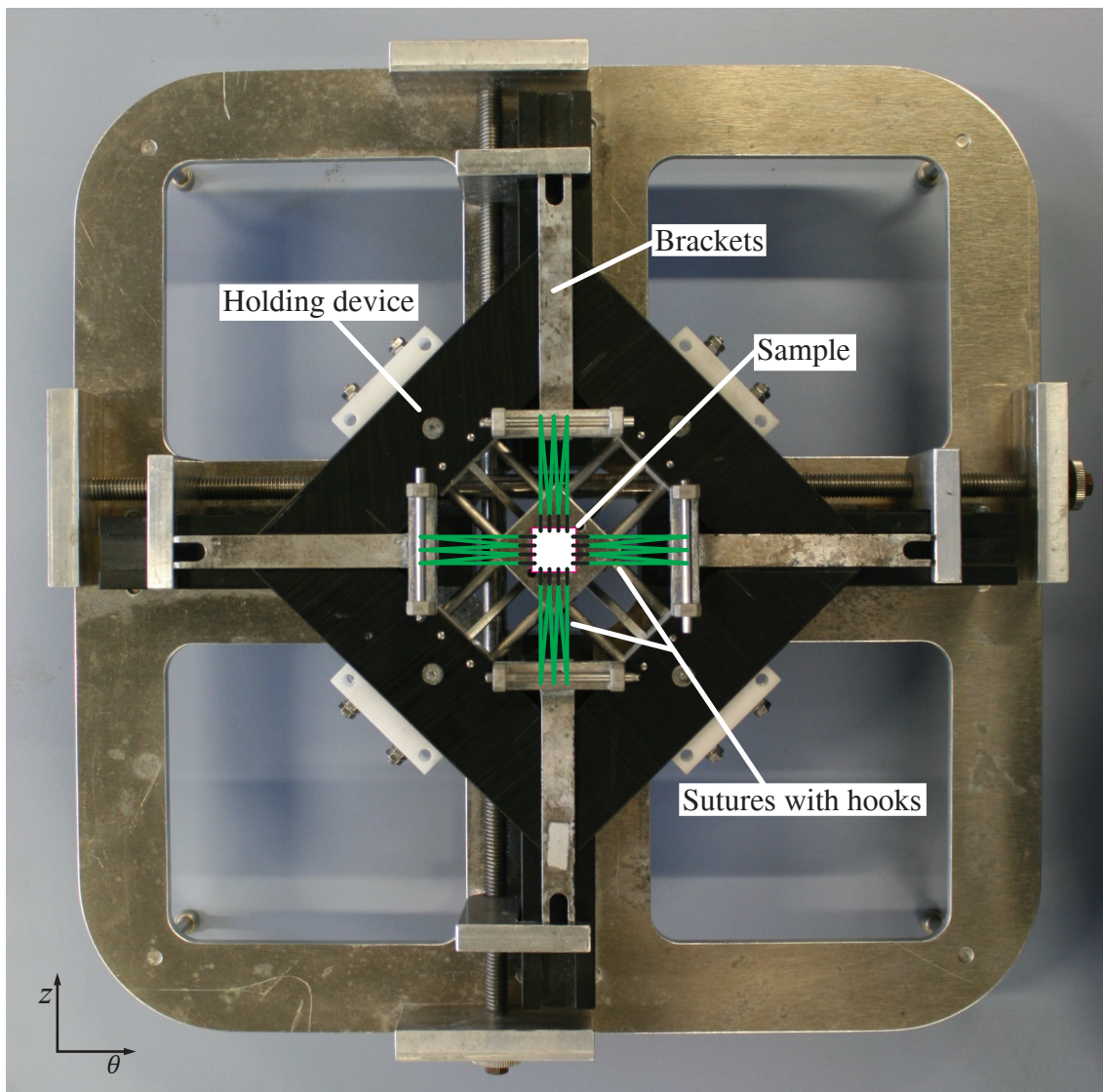Figure 2.9   Holding device with a schematic hooked sample placed in a trampoline fashion.

2.3.2 Preconditioning Tests

The preconditioning is important to have comparable measuring cycles, because during the dissection of the RCA, the blood pressure is not affecting the specimen. Therefore, the fibers pull themselves together, and the sample reaches a non-physiological state. To find out how long the sample needed to be rehydrated and how many preconditioning cycles were needed, tests were performed on the biaxial testing device and on the LAESIO testing device. The description of the biaxial testing device can be found in the work of Sommer et al. [15].

The biochemical preconditioning tests on the biaxial testing device were stretch controlled up to the stretch of 1.18 in both directions with a testing velocity of $v = 1\,\text{mm/min}$. The sample was pre-stretched with a force of $0.01\,\text{N}$ on every load cell and immediately afterwards the sample was stretched to $\lambda = 1.18$. This was repeated every 30 minutes. Between every measuring series the sample was kept loaded with a minimal force of $0.01\,\text{N}$ in both directions to prevent the sample from sagging. The first measuring series, with five test cycles, was performed at $t = 0\,\text{min}$ and the last measuring series at $t = 180\,\text{min}$. Figure 2.10 shows the schematic testing protocol.
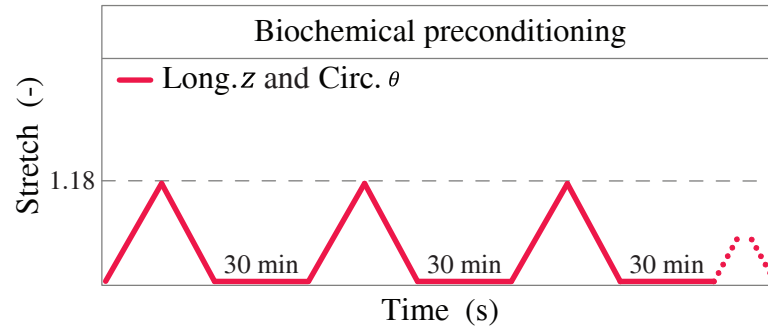
Figure 2.10   Stetch λ versus time test protocol during biochemical preconditioning. The testing started in a pre-stretched state with a force of $0.01\,\text{N}$ in both directions followed by 7 elongation cycle to $\lambda = 1.18$ with 30 minutes resting time loaded with a minimal force of $0.01\,\text{N}$ in both directions.

With the information gathered from the biochemical preconditioning test series, biomechanical preconditioning tests were performed with the LAESIO testing device. These tests were force controlled. The sample was rehydrating for 90 minutes in a relaxed state. Then, the sample was pre-stretched with a force of $0.01\,\text{N}$ on every load cell and immediately afterwards the test started and ten preconditioning cycles were performed to check how many cycles were needed in order that the sample was preconditioned. Between every measuring series, the sample was kept loaded with a minimal force of $0.01\,\text{N}$ in both directions to prevent the sample from sagging. In Figure 2.11, the schematic test protocol is shown.
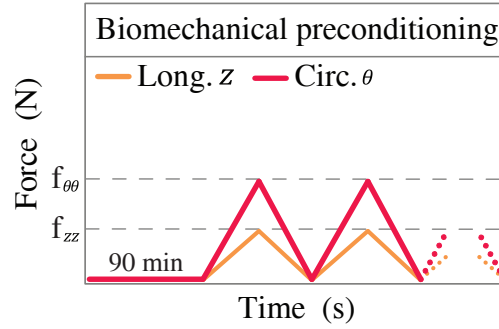
Figure 2.11 Schematic force F versus time test protocol during preconditioning. It
              started with 90 minutes resting time in an unloaded state. Then ten mea-
              suring cycles followed. f_{zz} : physiological load in the longitudinal direction,
              $f_{\theta\theta}$: physiological load in the circumferential direction.

2.3.3 Relaxation Tests

To determine viscoelastic features of the RCA quasi static relaxation tests were performed
with the LAESIO testing device. The schematic test protocol is displayed in Figure 2.12.
The sample was pre-stretched with a force of $0.01\,\mathrm{N}$ on every load cell and immediately
afterwards the sample was loaded up to the physiological state until the forces $f_{\theta\theta}$ and f_{zz}
were reached. Then the linear stages kept the position, so the sample could relax. Stress
relaxation describes how the sample relieves stress under constant strain. Another relax-
ation test was performed, where the sample was physiologically loaded and additionally the
stamp was indented with an indentation force of $F_{\mathrm{ind}} = 2\,\mathrm{N}$ and kept constant. The linear
stages kept the position, so the sample could relax and the relaxation time was measured.

Figure 2.12 Force F versus time test protocol during relaxation. The sample was loaded
              up to the physiological state and the linear stages kept the position. f_{zz} :
              physiological load in the longitudinal direction, $f_{\theta\theta}$: physiological load in
              the circumferential direction.

2.3.4 Indentation Tests

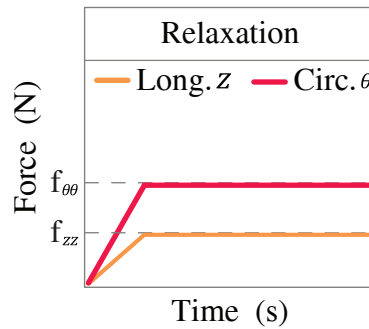In total, eight samples were tested during the indentation tests. In Table 2.1 all samples are listed with the stamp information, including the stamp indentation angle ι and the stamp indentation force F_{ind}. The sample parameters include the measured length of the edges of the squared sample and the mean thickness, assuming that every edge has the same length.

Table 2.1   Indentation test samples. The stamp parameters of every sample with the stamp indentation angle ι and the stamp force F_{ind}. The sample parameters with the measured length L of the edges and the mean measured thickness T_0.

		Stamp parameters		Sample parameters	
Series	Sample	ι [°]	F_{ind} [N]	L [mm]	T_0 [mm]
A	I	0	2	8	0.93
	II			8	1.05
B	III	0	1	8	0.85
	IV			9	1.03
C	V	90	2	8	0.84
	VI			7.5	0.93
D	VII	90	1	9.5	1.09
	VIII			8	0.72

Figure 2.13 shows the whole schematic testing procedure. The optimized test protocol consists of three units: the preconditioning, the first measuring series with the indentation and the second measuring series. To assemble those three units back together the minimal force between every cycle is set to $0.01\,\text{N}$ and to prevent the sample from sagging. During the first testing unit, the preconditioning, shown in Figure 2.13 *Unit A*, the sample was cyclic stretched to the physiological state. During the preparation phase, the sample got dehydrated. Therefore, the sample needed about 90 minutes in a relaxed state, to re-hydrate before the test could start. After that, the sample was manually pre-loaded with $0.01\,\text{N}$ on every linear stage. This setup is called the reference configuration. In this state, as shown in Figure 2.14, the reference distance X_z and X_θ for the global deformation in both directions was measured manually using the VE. The author assumes that the hooks, the suture and the brackets are stiff. Therefore, the movement of the linear stages is the same as the movement of the connection point between the hooks and the sample. For illustrative purposes, the reference length X_θ in the circumferential direction is shown in Figure 2.14, with a red line. For the local deformation, patterns of high contrast in the middle of the sample were measured the distances in the circumferential and longitudinal directions during the entire test. Figure 2.14 shows that the displacement in the longitudinal direction was measured with the distance between pattern 2 and pattern 8 and the distance between pattern 4 and 6 measured the displacement in the circumferential direction.

Unit B has two parts. It starts with *Unit B.1*, the first measuring series, shown in Figure

2.13 *Unit B.1*, comprising five consecutive measuring cycles where the sample was physiologically loaded and the mechanical response of the vital sample was measured. After the first measuring series the squareed sample was again physiologically loaded, as presented in Figure 2.13 *Unit B.2*. During this unit the stamp was induced in one of the angles described in Figure 2.7. The positions of the linear stages did not change during the indentation. The indentation of the stamp forces the sample to a supra-physiologically state. The stamp stayed induced for 15 minutes and was kept on a constant force.

The third and last testing unit was again a measuring series, shown in Figure 2.13 *Unit C*, consisting of five consecutive measuring cycles were the sample was physiologically loaded and the mechanical response of the damaged sample was measured. The comparison between the first measuring series from *Unit B.1* and the second measuring series from *Unit C* showed the softening because of the stent indentation.

Softening of the tissue can be recognized by rising stretches of the tissue under physiological load in the damaged state. This was realized by comparing the means of the maximal measured stretch λ and stress σ in the vital and the damaged state of the sample. Therefore $\Delta\lambda$ was used, to define the difference between the stretch of the vital and the damaged state of the sample. In general, circumferential and axial stresses increase with increasing stretch. The difference in stress between the vital and the damaged state of the sample was described as $\Delta\sigma$.
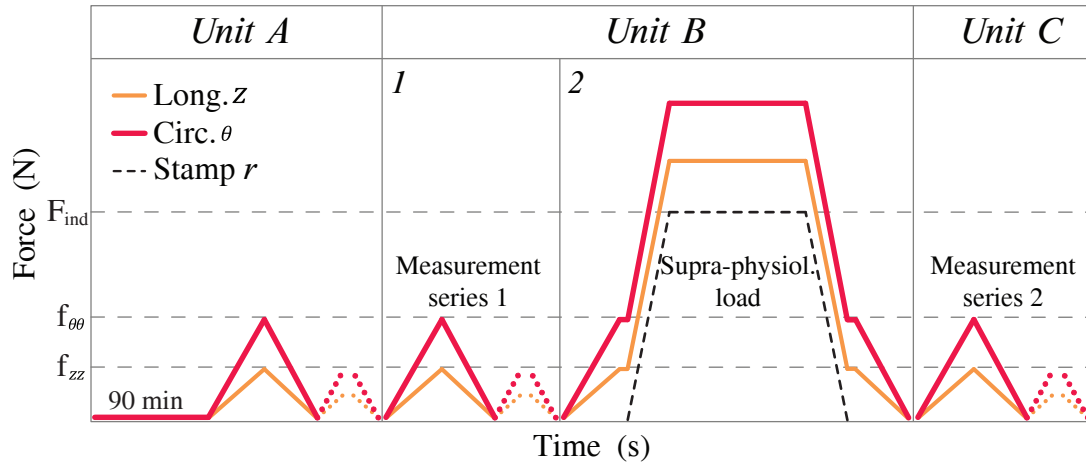
Figure 2.13 Schematic force F over time test protocol for the indentation tests with the three units. In *Unit A* the preconditioning was shown. *Units B.1* displays the first measuring series and *Units B.2* the stamp indentation. *Unit C* shows the second measuring series. z: longitudinal direction, θ: circumferential direction, r: radial direction, f_{zz}: physiological load in the longitudinal direction, $f_{\theta\theta}$: physiological load in circumferential direction, F_{ind}: stamp indentation force.
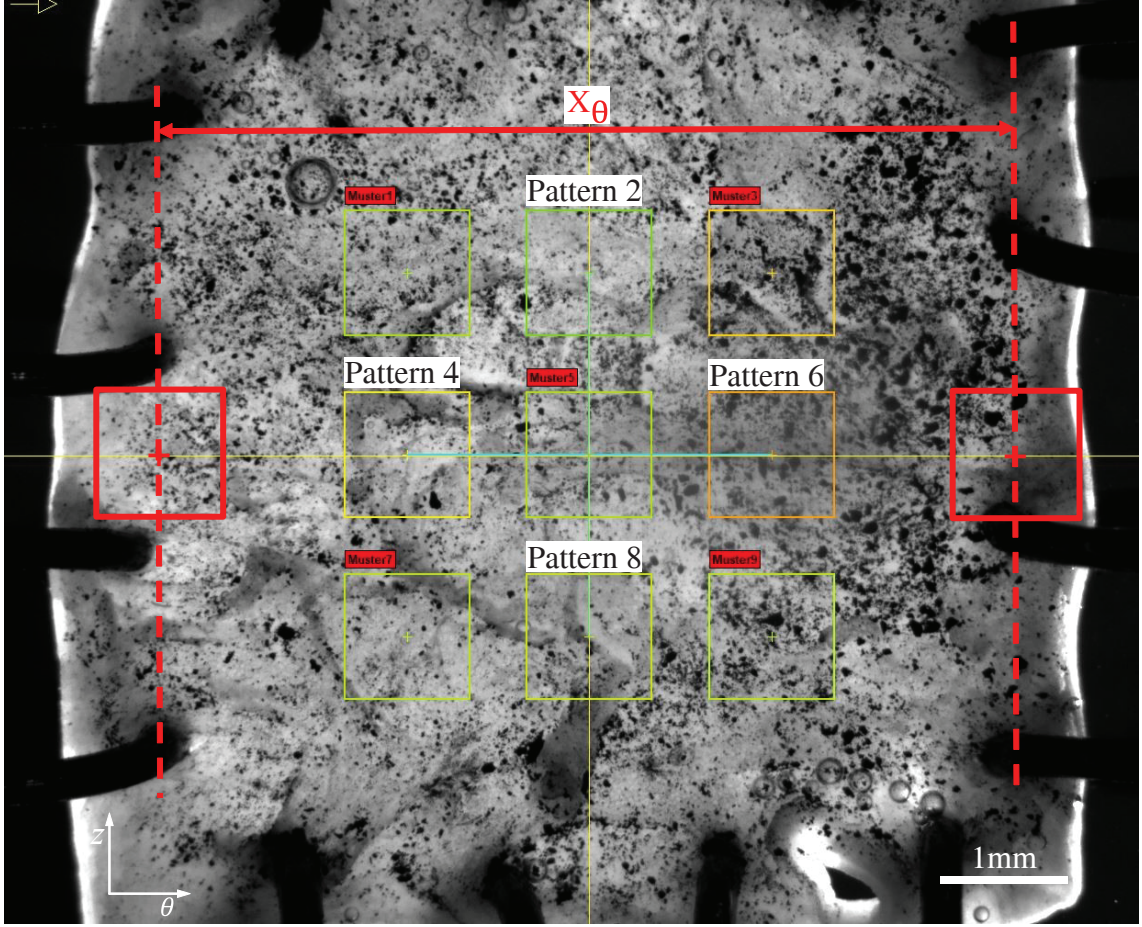
Figure 2.14   Reference configuration of the sample, where X_θ denotes the reference length in the circumferential direction.

2.4 Experimental Data Acquisition Processing

To plot the results, the Cauchy stress and the global stretch were calculated using the following formulas. First, the mean forces $\bar{f}_z$ and $\bar{f}_\theta$ were computed according to

$$\bar{f}_z = \frac{|f_z^+| + |f_z^-|}{2} \qquad \text{and} \qquad \bar{f}_\theta = \frac{|f_\theta^+| + |f_\theta^-|}{2} \quad, \tag{2.3}$$

where f_z and f_θ are the current forces in positive and negative axis direction. The author assumes that the hooks, the suture and the brackets are stiff. Therefore, the movement of the linear stages was the same as the movement of the connection points on the sample. The local displacement data from the VE could not be used due to measuring problems because of the sample size and the infinitesimal movements of the local field. Therefore,

the global displacement data u_z and u_θ from the linear stages were summed up as follows

$$u_z = |x_z^+| + |x_z^-| \qquad \text{and} \qquad u_\theta = |x_\theta^+| + |x_\theta^-| \quad , \qquad (2.4)$$

in which x_z and x_θ are the current positions of the linear stages in positive and negative axis direction counting from a zero point on the linear stages set in the pre-stretched state. The displacement was used to compute the global stretches λ_z and λ_θ according to

$$\lambda_{zz} = 1 + \frac{u_z}{X_z} \qquad \text{and} \qquad \lambda_{\theta\theta} = 1 + \frac{u_\theta}{X_\theta} \quad , \qquad (2.5)$$

with X_z and X_θ as the distance between the hooks in the reference state. Those were measured, as described in Section 2.3.4, with the help of the VE. The last step of the post-test data processing was to calculate the normal components of the Cauchy stresses σ_{zz} and $\sigma_{\theta\theta}$ according to

$$\sigma_{zz} = \frac{f_z}{L\,T_0}\,\lambda_{zz} \qquad \text{and} \qquad \sigma_{\theta\theta} = \frac{f_\theta}{L\,T_0}\,\lambda_{\theta\theta} \quad , \qquad (2.6)$$

where λ_{zz} and λ_θ represent the previously calculated stretches in the longitudinal and circumferential direction, respectively, and L is the length of one edge of the squared sample, assumed that every edge has the same length. The thickness of the sample is denoted by T_0, measured with a VE, as described in Section 2.3.1.

2.5 Microstructural Analysis

Within the microstructural analysis the collagen fibers of five porcine RCA samples, i.e. one native sample and four damaged samples, were investigated. The damaged samples were tested, as described in Section 2.3.4 with a different stamp force and stamp orientation, shown in Table 2.2, where in sample L1 and L2 the stamp was indented in the longitudinal direction with the force of 1 and 2 N, respectively. In sample C1 and C2, the stamp was indented in the circumferential direction with the force of 1 and 2 N, respectively. To illustrate the elevation profile, a 3D-surface scan of every sample was additionally performed.

Table 2.2   Samples for the microstrutural analysis, with the specific stamp parameters including the stamp indentation angle ι and the stamp force F_{ind}.

Sample	ι [°]	F_{ind} [N]
N	no stamp indentation	
LI	0	1
LII	0	2
CI	90	1
CII	90	2

To analyze the microstructural vascular morphology of the RCA, in particular the orientation of the collagen fibers, a multiphoton microscope, specifically SHG imaging, was used. The three-dimensional collagen structure of the samples was identified by SHG imaging at the Core Facility Bioimaging of the Biomedical Center, Ludwig-Maximilians-Universität München, Germany. The structure scans were performed on a multi-photon SP8MP upright microscope (*SP8, Leica Microsystems; Mannheim, Germany*). Images were acquired using a water immersion lens (*HC IRAPO L 25x/1.00 W motCORR, Leica Microsystems; Mannheim, Germany*). For the SHG images the excitation wavelength of 880 nm was used generated from a pulsed InSight DS+ laser (*InSight DS+, Spectra Physics; California USA*). The backscattered signal was filtered with an AT 420/40 emission filter and a BS 488LPXR beam splitter to observe the collagen structure of the media and the adventitia. The detection of the backscattered signal was achieved using an external, non-descanned hybrid photo detector (HyD) in 8-Bit mode with an image pixel size of 100 nm, and frame accumulation of $x = 3$ width. Images were acquired using a water immersion lens (*HC IRAPO L 25x/1.00 W motCORR, Leica Microsystems; Mannheim, Germany*) with a working distance of 2.6 mm. The detection of elevation profiles of all lesions was achieved by performing 3D-surface scans on the specimens with the intima facing up. Confocal images were recorded in reflection mode with an internal conventional photomultiplier tube by using solid-state laser excitation at 488 nm. The image pixel size was set to 500 nm.

2.5.1 Sample Fixation and Optical Clearing

For the morphological analysis, the samples from Table 2.2 were used. The testing protocol for the native sample is shown in Figure 2.15. *Unit A*, the preconditioning, is the same as in Figure 2.13 *Unit A*, and is therefore described in Section 2.3.4. In *Unit B* the sample was manually preloaded with $0.01\,\text{N}$ on every linear stage and then again physiologically loaded. When the physiological state was reached, the linear stages kept their position. After $15\,\text{min}$ *Unit C* starts, where the tempered PBS solution in the tissue bath was changed to a $37\pm1.0°\text{C}$ warm $4\,\%$ formaldehyde solution to chemical fixate the native sample. After $360\,\text{min}$ the sample fixation was completed and the physiological state was preserved.

Figure 2.15　　Schematic force F over time test protocol for the indentation tests with the three units. *Unit A* shows the preconditioning. In *Units B* the sample was physiologically loaded and in *Unit C* the chemical fixation under physiological load was completed. z: longitudinal direction, θ: circumferential direction, f_{zz}: physiological load in the longitudinal direction, $f_{\theta\theta}$: physiological load in the circumferential direction.

For the damaged samples, the testing protocol is shown in Figure 2.16. *Unit A*, the preconditioning, is the same as in Figure 2.13 *Unit A*, and is therefore described in Section 2.3.4. In *Unit B* the sample was manually preloaded with $0.01\,\text{N}$ on every linear stage and then again physiologically loaded. When the physiological state was reached, the linear stages kept their position. Still in *Unit B* the stamp was indented in a specific angle described in Table 2.2. The stamp remained indented or $375\,\text{min}$ and was kept on a constant force. After $15\,\text{min}$ *Unit C* started, where the tempered PBS solution in the tissue bath was changed to a $37\pm1.0°\text{C}$ warm $4\,\%$ formaldehyde solution. After $360\,\text{min}$ chemical fixation was completed and the damaged state of the sample was preserved.
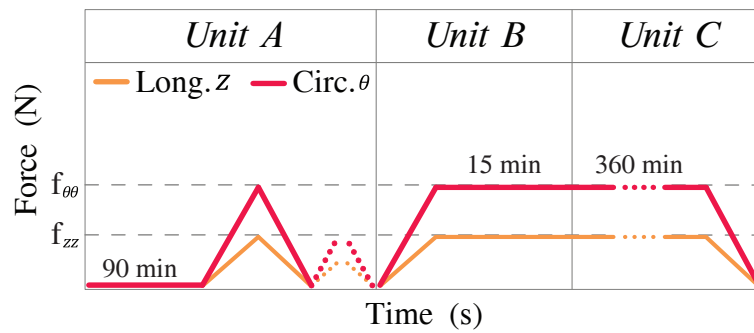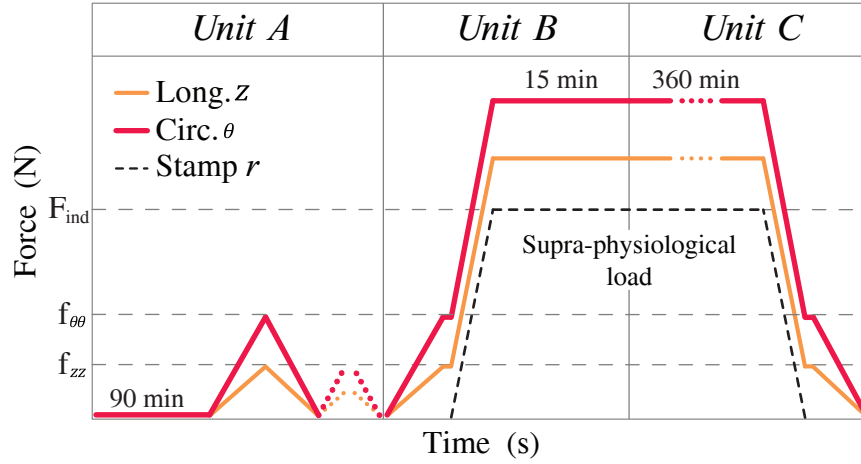
Figure 2.16   Schematic force F over time test protocol for the indentation tests with the
three units. *Unit A* shows the preconditioning. In *Units B* the sample was
physiologically loaded and the stamp was indented. *Unit C* displays the
chemical fixation of the sample under F_{ind}. z: longitudinal direction, θ: cir-
cumferential direction, τ: stamp indentation, f_{zz}: physiological load in the
longitudinal direction, $f_{\theta\theta}$: physiological load in circumferential direction,
F_{ind}: stamp indentation force.

The coronary arteries fixated under load, shown in Figure 2.17 are placed in a biopsy
cassette with four compartments (M508-Micromesh, Simport Scientific; Canada), as dis-
played in Figure 2.18. Underneath and on top of every sample a piece of biopsy foam pads
(Carl Roth; Karlsruhe, Germany) was placed to keep the sample in the actual flat shape,
because of the $4\,\%$ formaldehyde solution and optical clearing process the sample could
curl. This was necessary because for the SHG imaging flat samples were required.

    The samples were optical cleared using the protocol from Schriefl et al. [29]. First,
the samples were rinsed with phosphate-buffered saline to wash off the remaings of the
formaldehyde solution, and dehydrated using a graded ethanol series, comprising 50, 70,
95 and twice $100\,\%$ concentrated ethanol solutions with each step, lasting for $45\,\text{min}$. For
optical tissue clearing a solution of $1:2$ benzyl alcohol to benzyl benzoate (BABB) was
used. Each sample was initially dipped into a solution of $1:1$ ethanol : BABB for $4\,\text{h}$
before submerging them into a $100\,\%$ BABB solution, where they remained for at least
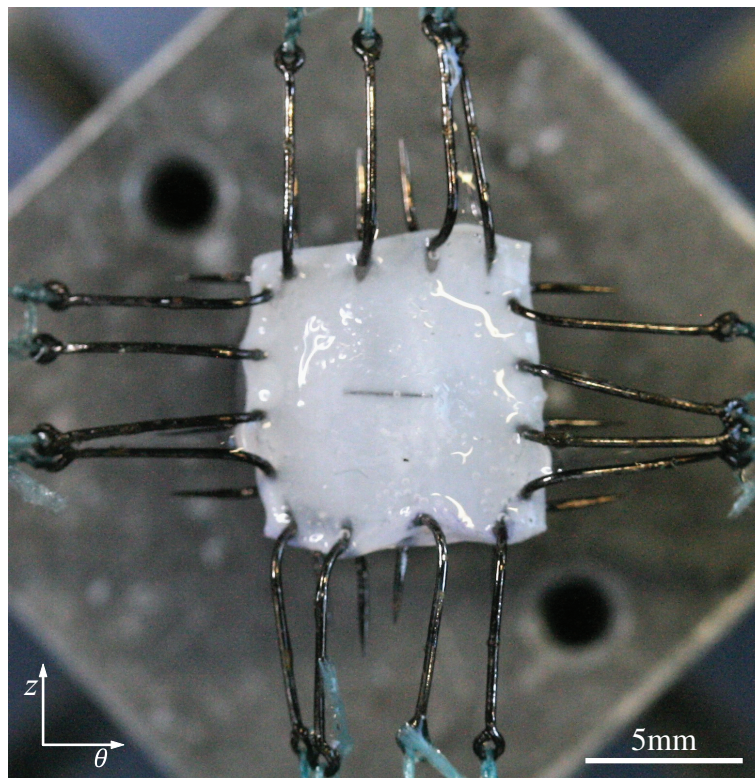$12\,\text{h}$ before imaging.

Figure 2.17   Chemical fixed sample with the indentation visible in the middle of the sample.
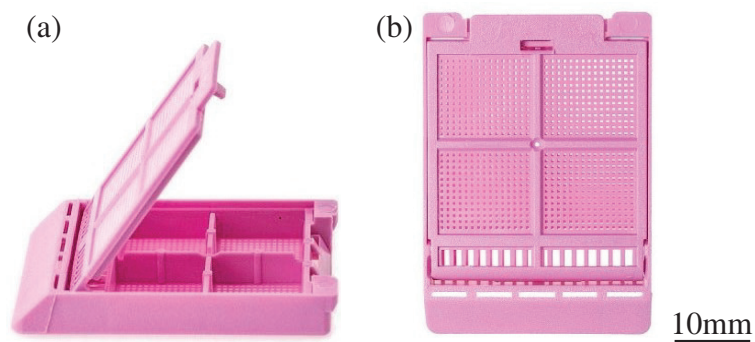

Figure 2.18   Biopsy cassette M508-Micromesh by Simport Scientific: (a) Side-view of the biopsy cassette with the four compartments visible; (b) top-view of the closed biopsy cassette.

2.5.2 Second–Harmonic Generation Imaging Protocol

The samples from Table 2.2 were investigated with the SHG microscopy. In Figure 2.19, the schematic cross section of a damaged sample is shown, where the stamp was indented at the angle of $\iota = 0°$. The origin lies in the center of the sample on the level t_v]. This means that the (θ, z)-plane lies on level t_v and the (θ, r)-plane lies in the center of the sample. For the determination of the layer-specific structure parameters, so-called in-plane image stacks must be created in the r-direction over the entire sample thickness. In addition, at least one out-of-plane scan of the same tissue area was performed in the (θ, z)-plane. The distance k_max denotes the distance between the middle of the lesion and the native part of the sample. The native part of the sample was defined as the region right before the curvature of the lesion started, marked with a red line in Figure 2.19. Since the compression of the tissue of the damaged sample increased along k_max, it has had to be expected that there will also be changes in the fiber distribution depending on the distance to the lesion. Thus, the values of the structural parameters should also change within k_max. The compression λ_r of the sample is defined by the nonlinear function

$$\lambda_r = 1 - \frac{T_0 - t(k)}{T_0} \quad , \tag{2.7}$$

where T_0 is the wall thickness before the testing and $t(k) \in [t_\mathrm{min}, t_\mathrm{v}]$ is the compressed wall thickness with $k \in [0, k_\mathrm{max}]$ representing the distance between the center of the lesion and the virgin tissue.
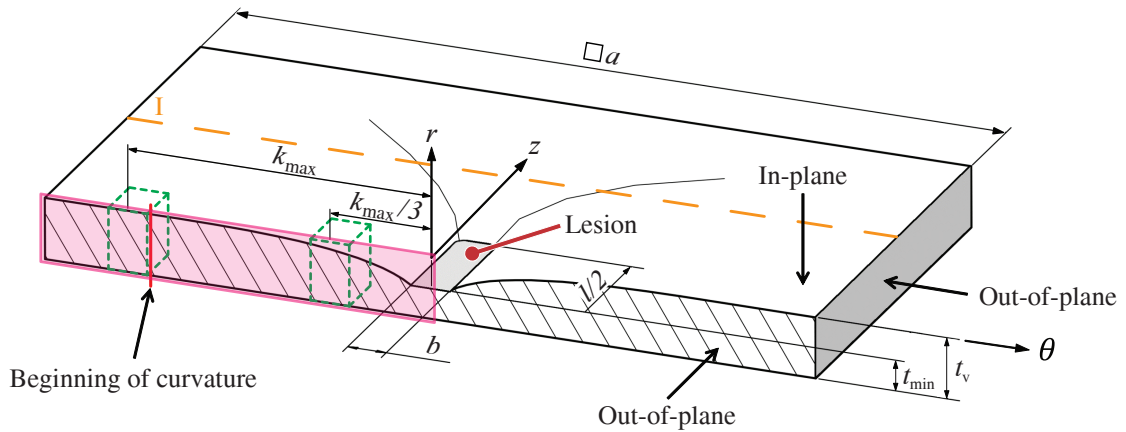
Figure 2.19   Schematic cross section of a damaged sample, where the stamp indented at the angle $\iota = 0°$. a: size of the sample, t_v: sample thickness, t_min: sample thickness in the middle of the lesion, b: stamp width, l: length of the stamp, k_max: distance between the middle of the lesion and beginning of the curvature. Adapted and modified from M. A. Geith, Institute of Biomechanics, Graz University of Technology.

The first step was to place the sample on a prepared custom object carrier, which consisted of an object carrier with a small basin on top of it. The basin was a washer (*iglidur W300, igus; Köln, Germany*) with an inner diameter of $10\,\mathrm{mm}$, an outer diameter of $18\,\mathrm{mm}$ and a thickness of $1\,\mathrm{mm}$ glued on top of the object carrier with nail polish, shown in Figure 2.20. The sample was placed in the basin and filled with BABB solution and closed with a coverslip. After ensuring that there were no air bubbles in the closed basin, the coverslip was sealed with nail polish because the water immersion lens should not be in contact with BABB. This was done with the samples for the in-plane and out-of-plane scans.
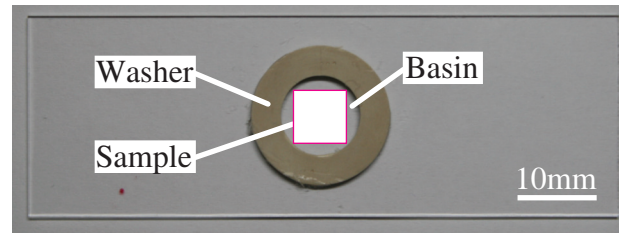

Figure 2.20   Object carrier with the basin and a schematic sample for the in-plane scans.

To acquire the images, the object carrier with the flat squared sample was then placed in the microscope. First the in-plane stack scans were created, as presented in Figure 2.19, with green cuboids. The first stack scan was performed at a distance $k_{\mathrm{max}}/3$ from the (z, r)-plane, which is the same as the center of the sample, in the *r*-direction starting at the level *T* through the whole sample. The side length of every image is $355\,\mathrm{nm}$. A second identical stack scan was performed at a distance k_{max} from the (z, r)-plane. The distance of the individual images in the *r*-direction is $5\,\mathrm{\mu m}$. The description of the in-plane scans can be found in Table2.3. As an illustration of the sample geometry, a 3D-surface scan of every sample in the (θ, z)-plane with low resolution was performed, as listed in Table2.3. These scans were performed using the reflection mode of the confocal microscope. This scans can not show the sample thickness, because only the light reflected from the surface is recorded.

To acquire the out-of-plane scans the sample was cut through at the (θ, r)-plane, as shown in Figure 2.19, and parallel in a distance of $2\,\mathrm{mm}$ marked with an orange dashed line I. This strip was placed on the object carrier with the (θ, r)-plane facing to the lens. The basin was then filled with BABB, closed with a coverslip and then sealed. In total, one mosaic out-of-plane scan, as listed in Table2.3, was created, which is illustrated in Figure 2.19, with the pink area. The mosaic out-of-plane scan was cropped into two out-of-plan images for the virgin and the damaged part, which corresponds to the distance $k_{\mathrm{max}}/3$ and k_{max} from the center of the sample, respectively.

While the in-plane stack scan of the virgin part is orthogonal to the intima, the damaged tissue tends to bulk due to the stamp indentation. Therefore, all SHG images of the in-plane z-stack and the out-of-plane scans at the distance $k_{\mathrm{max}}/3$ had to be rearranged perpendicular to the tangent laying on the intima by tilting all images with the angle measured in the out-of-plane images. This was archived by using the `reslice` and `transform` commands in Fiji.

The described scans were acquired alternately with all four damaged samples. For the investigation of the native sample, one in-plane scan and one out-of-plane scan was performed. Further an in-plane mosaic scan was captured for the illustration of the collagen fiber orientations in the media and the adventitia.

Table 2.3   Overview of the performed microstructural analysis scans for every sample.

Amount of scans	Scan description	Direction	Resolution
1	3D-surface	(θ, z)-plane	low
2	In-plane stack	r	high
1	Merged out-of-plane	(θ, r)-plane	high

2.6 Fiber Dispersion

The general fiber orientation, described by Holzapfel et al. [22], who introduced the coordinate system characterized by the unit vectors $\mathbf{e}_1$, the circumferential direction, $\mathbf{e}_2$, the longitudinal direction and $\mathbf{e}_3$, the radial direction. The coordinate system is shown in Figure 2.21(a), with the unit vector $\mathbf{N}$ representing the general fiber orientation, which is defined by the two angles $\Phi \in [0, 2\pi]$ and $\Theta \in [-\pi/2, \pi/2]$ as the in-plane and out-of-plane angle, respectively. Additionally, the two structural parameters κ_{ip} and κ_{op} are introduced, which define the fiber dispersion.
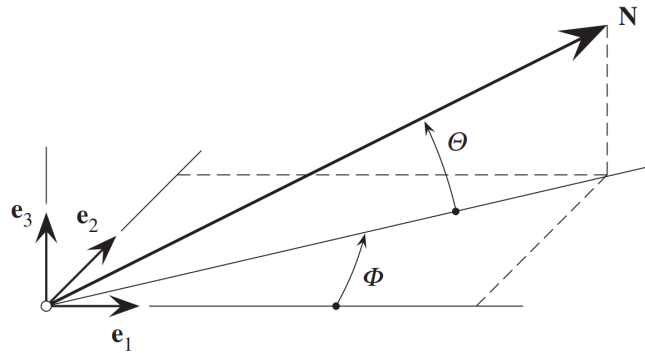

Figure 2.21   General fiber orientation represented by the unit vector $\mathbf{N}$ and defined by the two angles Φ and Θ, with respect to the Cartesian unit basis vectors $\mathbf{e}_1$, $\mathbf{e}_2$ and $\mathbf{e}_3$ [22].

The in-plane and out-of-plane collagen fiber orientations were fitted using a bivariate von Mises distribution $\rho(\Phi, \Theta) = \rho_{\mathrm{ip}}(\Phi)\,\rho_{\mathrm{op}}(\Theta)$ for the probability density ρ of $\mathbf{N}$, where the in-plane and out-of-plane dispersion are independent [29]. The probabilities are defined as

$$\rho_{\mathrm{ip}}(\Phi) = \frac{\exp[a\,\cos 2(\Phi \pm \alpha]}{I_0(a)} \qquad \text{and} \qquad \rho_{\mathrm{op}}(\Theta) = 2\sqrt{\frac{2b}{\pi}}\frac{\exp[b(\cos 2\Theta - 1)]}{\mathrm{erf}(\sqrt{2b})}, \quad (2.8)$$

where $\rho_{\mathrm{ip}}(\Phi) = \rho_{\mathrm{ip}}(\Phi + \pi)$ and $\rho_{\mathrm{op}}(\Theta) = \rho_{\mathrm{op}}(-\Theta)$ describe the in-plane and out-of-plane dispersion, respectively. In (2.8), a and b are constant concentration parameters, which define the shape of the von Mises distribution and $I_0(a)$ is the modified Bessel function of the first kind of order 0. The angle α is defined as the angle between the mean fiber direction and the circumferential direction $\mathbf{e}_1$ and erf is the error function.

The structural parameter κ_{ip} in the (θ, z)-plane (defined in Figure 2.19) is defined as

$$\kappa_{\mathrm{ip}} = \frac{1}{2} - \frac{I_1(a)}{2I_0(a)}, \qquad (2.9)$$

where I_0 and I_1 are the modified Bessel functions of the first kind of order 0 and 1, respectively. Important to note is that κ_{ip} is restricted by $0 \leq \kappa_{\mathrm{ip}} \leq \frac{1}{2}$. If $a \to \infty$ the dispersion parameter $\kappa_{\mathrm{ip}} \to 0$ which indicates that the fibers are aligned perfectly. If $a \to 0$ the dispersion parameter $\kappa_{\mathrm{ip}} \to \frac{1}{2}$ which shows that the fibers are dispersed equally.

The structural parameter κ_{op} in the (θ, r)-plane (defined in Firgure 2.19) is defined as

$$\kappa_{\mathrm{op}} = \frac{1}{2} - \frac{1}{8b} + \frac{1}{4}\sqrt{\frac{2}{\pi b}}\frac{\exp(-2b)}{\mathrm{erf}(\sqrt{2b})}. \qquad (2.10)$$

Important to note is that κ_{op} is restricted by $0 \leq \kappa_{\mathrm{op}} \leq \frac{1}{2}$ and if $b = 0$ then $\kappa_{\mathrm{op}} = \frac{1}{3}$. If $b \to \infty$ the dispersion parameter $\kappa_{\mathrm{ip}} \to 0$ which indicates that the fibers are aligned perfectly. To determine the fiber angle Φ, the structural parameters κ_{ip} and κ_{op} in-plane stack and out-of-plane scans were used. The images were acquired following Section 2.5.2.

The fiber angle Φ was extracted with the plug-in *AngleExtraction* for Fiji (*Fiji, ImageJ, Ashburn, VA, USA*) which was implemented by Zehentner [30]. The plug-in creates intensity plots of fiber orientation and produces a table with the related intensities. The data got normalized and wedge filtered with a wedge width of $3°$, which was used due to noisy images. The structural parameters α, κ_{ip} and κ_{op} of the tested samples were determined from the in-plane and out-of-plane SHG images using MATLAB (*R2015b, The MathWorks; Natick, MA, USA*), according to Schriefl et al. [29].

3 Results

3.1 Biochemical and Biomechanical Preconditioning

Figure 3.1 shows representative results of the biochemical preconditioning tests at an equibiaxial stretch of 1.18. During preconditioning, with increasing cycle number, stress softening was observed in the longitudinal and the circumferential direction, which are represented in Figure 3.1(a) and Figure 3.1(b), respectively. The mechanical response shows a difference between the first testing cycle (dashed black curve) at $t = 0$ min and the last testing cycle (solid black curve) at $t = 180$ min. The sample had the same mechanical behavior after 30 min. To make sure that the sample was rehydrated and biochemical preconditioned it was kept at 37°C for 90 min in an unloaded state.
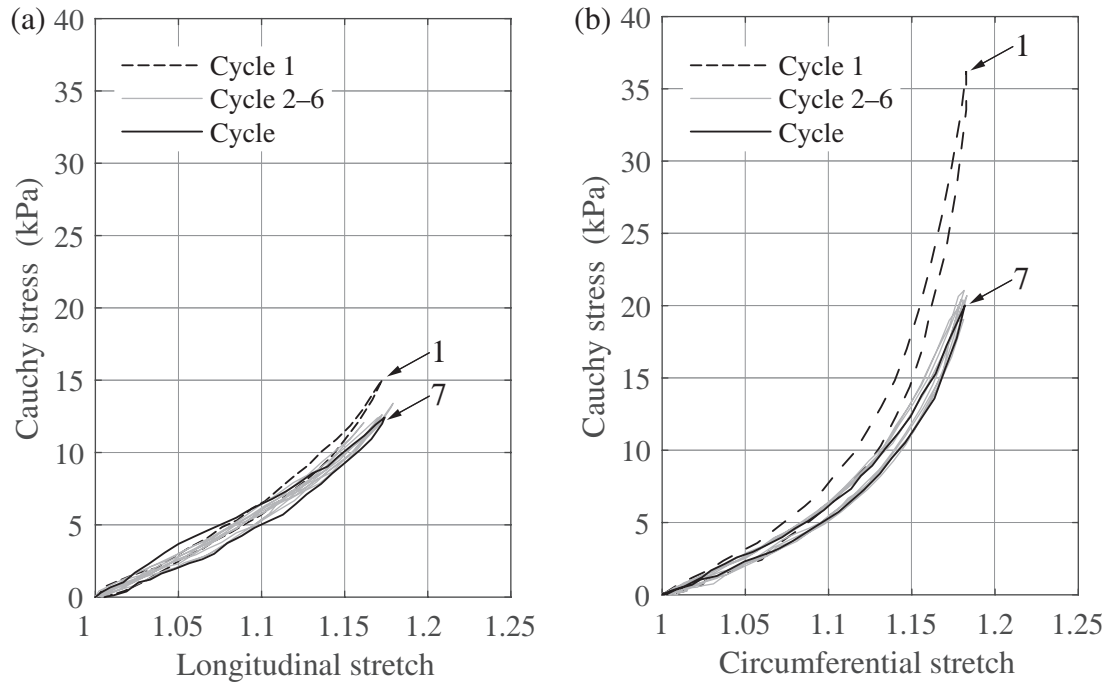

Figure 3.1   Representative biochemical preconditioning behavior at 1.18 stretch. The first (dashed curve) and the last (seventh, solid curve) cycle are indicated with arrows. Mechanical response (a) in the longitudinal direction and (b) in the circumferential direction.

31

For the RCA three preconditioning cycles were needed, which showed the results from the biomechanical preconditioning tests. Figure 3.2(a) and Figure 3.2(b) show the representative mechanical response of a vital sample in the longitudinal and the circumferential direction, respectively. During cyclic preconditioning, none or minimal changes in the mechanical response are indicated by the small shift between the first testing cycles (dashed curve) and the third cycle (solid curve). This mechanical behavior was checked after the preconditioning and was found for every sample.
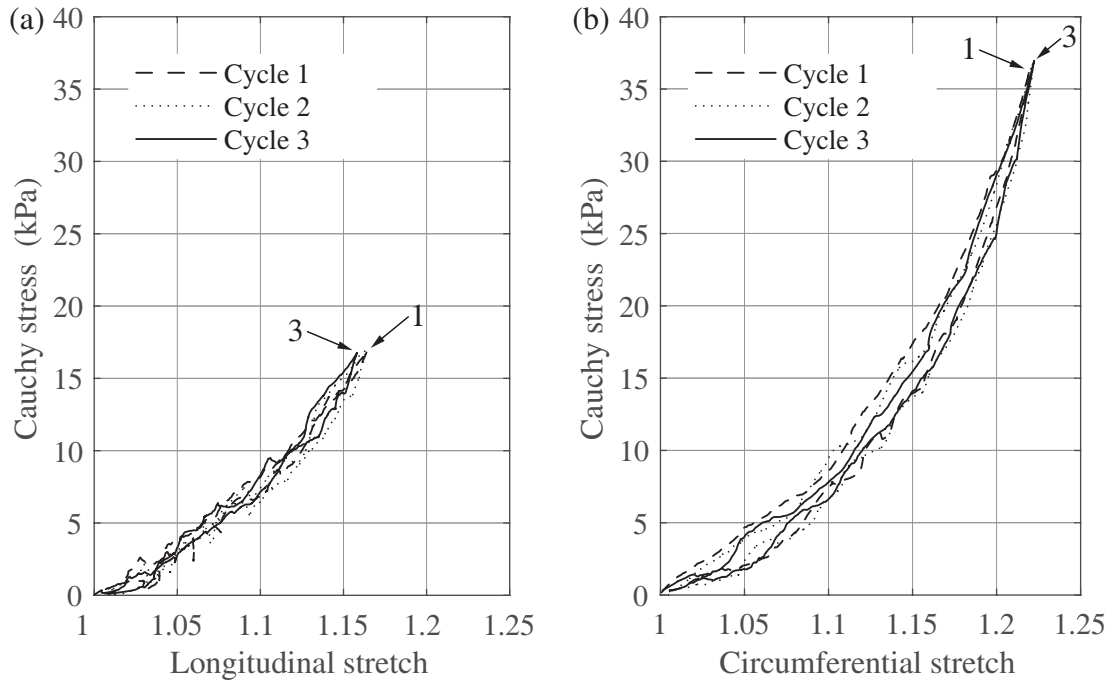

Figure 3.2   Representative biomechanical preconditioning prior to every test under physiological load. The first and the last (third) cycle are indicated with arrows. Mechanical response (a) in the longitudinal direction and (b) in the circumferential direction.

3.2 Relaxation Tests

Representative relaxation curves of the RCA under physiological load are shown in Figure 3.3(a), where the Cauchy stress as a function of time in the longitudinal (gray curve) and the circumferential direction (black curve) is plotted. The stretch increases rapidly at the beginning until after 67 sec the physiological stress of 20 kPa in the longitudinal and 40 kPa in the circumferential direction is reached. Immediately after the stress dropped in both directions and gradually decreased until it stabilized after 15 min. The stress decreased by approximately 15 and 20 % in the longitudinal and the circumferential direction, respec-

tively. The curves in Figure 3.3(b) present the representative relaxation behavior of RCA under supra-physiological load, which is achieved with the stamp indenting. When the indentation force of $F_{\text{ind}} = 2\,\text{N}$ is reached, a maximum stress of $101\,\text{kPa}$ in the longitudinal and $203\,\text{kPa}$ in the circumferential direction occurred. Holding the indentation load constant, the stress dropped immediately. Further it decreased gradually until it stabilized after $15\,\text{min}$. The stress decreased by approximately 6 and $13\,\%$ in the longitudinal and the circumferential direction, respectively. Both relaxation tests showed the viscoelastic behavior of the RCA tissue and that after $15\,\text{min}$ almost no difference in the stresses occurred.
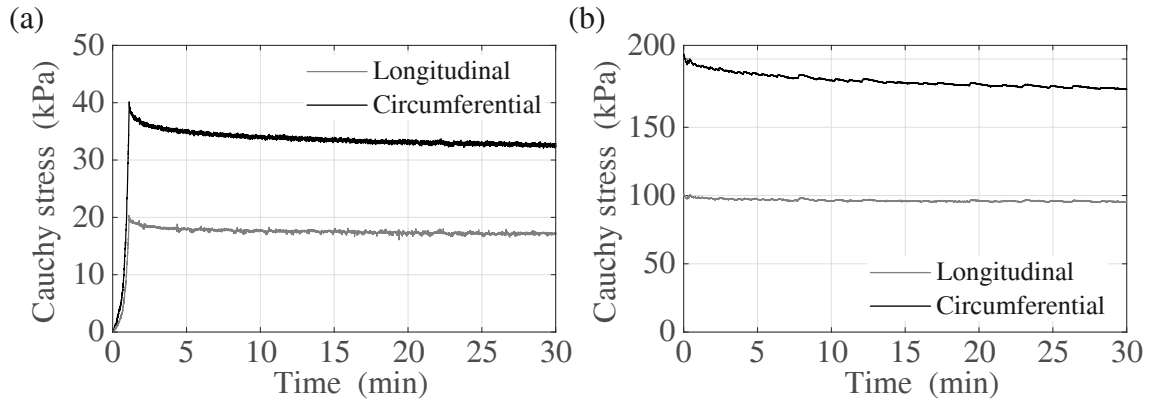
(a)

(b)

Figure 3.3   Representative relaxation behavior of the RCA: (a) with applied physiological load; (b) with supra-physiological load with an indentation force of $F_{\text{ind}} = 2\,\text{N}$. The normal Cauchy stress components in the longitudinal direction and the circumferential direction are indicated in gray and black, respectively.

3.3 Indentation Tests

The curves of the vital sample exhibited a nearly elastic behavior, which could be seen in the small hysteresis. The curves of the damaged sample exhibited a nearly elastic behavior as well. Typically, for soft collagenous tissue, the load deformation behavior is highly nonlinear, with pronounced stiffening at higher stresses in the circumferential direction [5]. In the longitudinal direction, a nearly linear behavior is observed. The anisotropic behavior of the coronary arteries can be seen in comparison of the two directions.

The mechanical behavior of the tested samples is presented in the following Cauchy stress-stretch plot. The dotted curves show the mean of the mechanical response of the vital sample. The light gray curves in the background show the measured data. In comparison, the solid curves represent the mean of the mechanical response of the damaged sample and the gray area in the background shows the measured data. The comparison of the vital and the damaged sample makes the material softening visible. This counts for all of the following Cauchy stress-stretch plots.

Figure 3.4(a) shows the mechanical response in the longitudinal direction, while Figure 3.4(b) shows the mechanical response in the circumferential direction of sample AII. Both plots are representative for testing series A with the stamp parameters from Table 2.1. This sample was tested with the stamp indenting at the angle $\iota = 0°$ and with the force $F_{\mathrm{ind}} = 2\,\mathrm{N}$. Figure 3.4(a) displays the softening in the longitudinal direction, indicating no significant softening. The severe softening of the tissue in the circumferential direction can be seen in Figure 3.4(b). This sample showed anisotropic behavior, with a stiffer response in the longitudinal than in the circumferential direction.
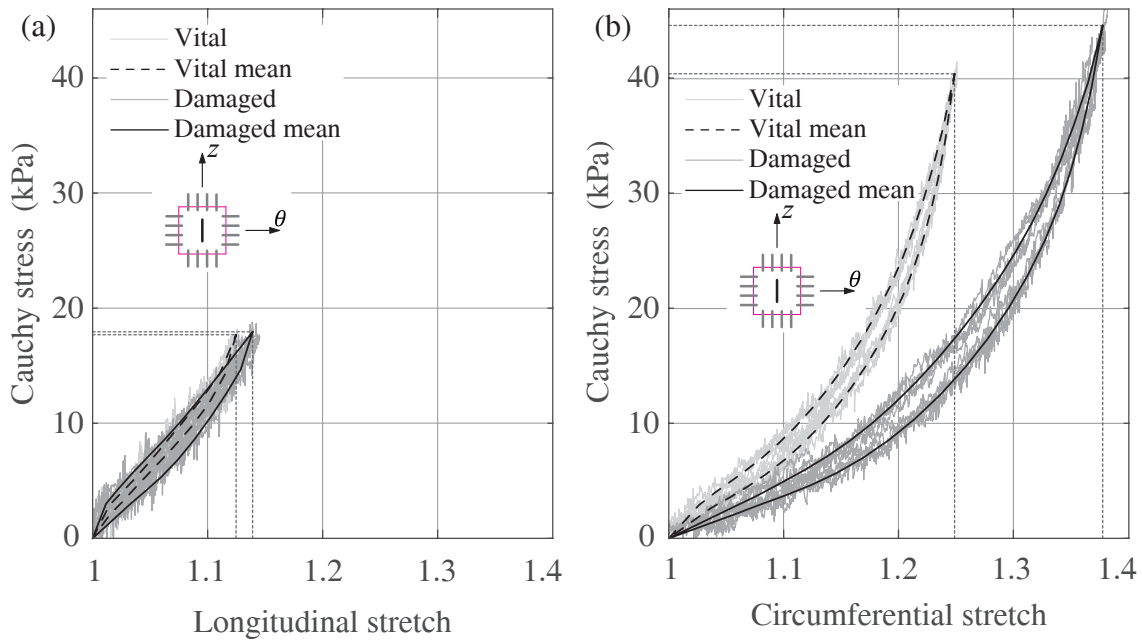

Figure 3.4   Representative Cauchy stress vs. stretch plots of sample AII with the stamp indenting at the angle $\iota = 0°$ and with the force $F_{\mathrm{ind}} = 2\,\mathrm{N}$. The mechanical response under physiological load of the vital and the damaged sample are indicated with the dashed and the solid black curve, respectively. Mechanical response (a) in the longitudinal and (b) in the circumferential direction.

Figure 3.5(a) shows the mechanical response in the longitudinal direction, while Figure 3.5(b) shows the mechanical response in the circumferential direction of sample BIV. Both plots are representative for testing series B with the stamp parameters from Table 2.1. This sample was tested with the stamp indenting at the angle $\iota = 0°$ with the force $F_{ind} = 1\,N$. Figure 3.5(a) shows that there is no significant softening of the tissue in the longitudinal direction. Because of the stamp orientation and the force of only $1\,N$ no softening occurred. Figure 3.5(b) displays the pronounced softening of the tissue in the circumferential direction. Sample BIV showed anisotropic behavior with a slightly stiffer response in the longitudinal than in the circumferential direction.

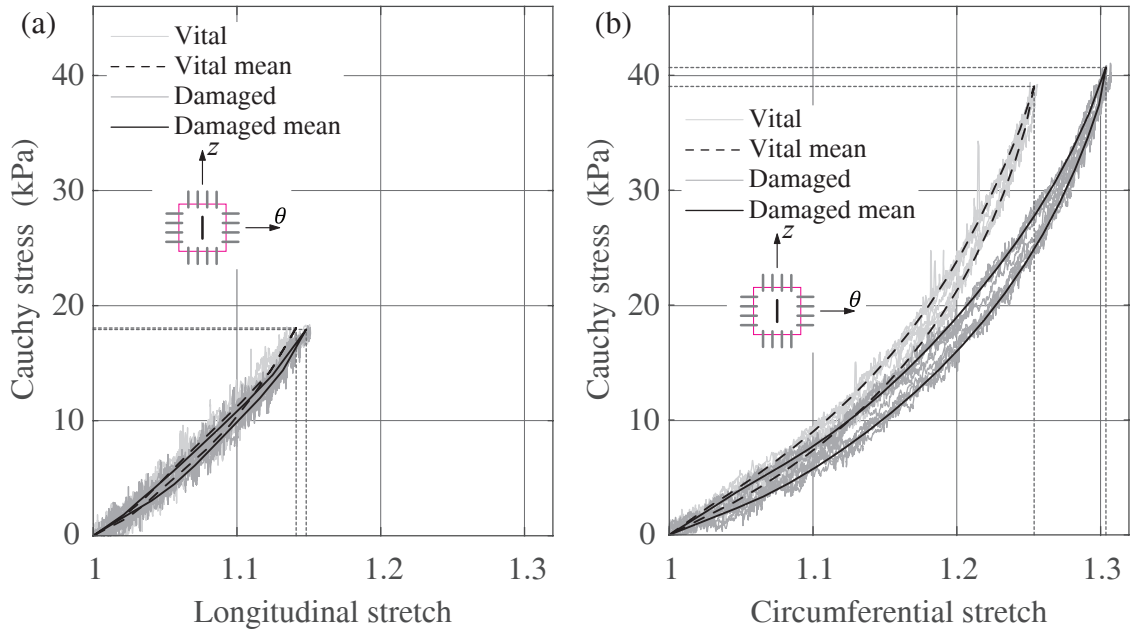Figure 3.5 Representative Cauchy stress vs. stretch plots of sample BIV with the stamp indenting at the angle $\iota = 0°$ and with the force $F_{ind} = 1\,N$. The mechanical response under physiological load of the vital and the damaged sample is indicated with the dashed and the solid black curve, respectively. Mechanical response (a) in the longitudinal and (b) in the circumferential direction.

Figure 3.6(a) shows the mechanical response in the longitudinal direction, while Figure 3.6(b) shows the mechanical response in the circumferential direction of sample CVI. Both plots are representative for testing series C with the stamp parameters from Table 2.1. This sample was tested with the stamp indenting at the angle $\iota = 90°$ with the force $F_{\text{ind}} = 2\,\text{N}$. The serious softening in the longitudinal direction is recognizable in Figure 3.6(a). In Figure 3.6(b) a critical softening of the tissue in the circumferential direction can be seen. Anisotropic behavior can be identified with a stiffer response in the longitudinal than in the circumferential direction.

Figure 3.6   Representative Cauchy stress vs. stretch plots of sample CVI with the stamp indenting at the angle $\iota = 90°$ and with the force $F_{\text{ind}} = 2\,\text{N}$. The mechanical response under physiological load of the vital and the damaged sample is indicated with the dashed and the solid black curve, respectively. Mechanical response (a) in the longitudinal direction and (b) in the circumferential direction.

Figure 3.7(a) shows the mechanical response in the longitudinal direction, while Figure 3.7(b) shows the mechanical response in the circumferential direction of sample DVII. Both plots are representative for testing series D with the stamp parameters from Table 2.1. This sample was tested with the stamp indenting at the angle $\iota = 90°$ with the force $F_{\mathrm{ind}} = 1\,\mathrm{N}$. Figure 3.7(a) shows notable softening of the tissue in the longitudinal direction. The significant softening in the circumferential direction is shown in Figure 3.7(b). Sample DVII showed an anisotropic behavior with a stiffer response in the longitudinal direction.
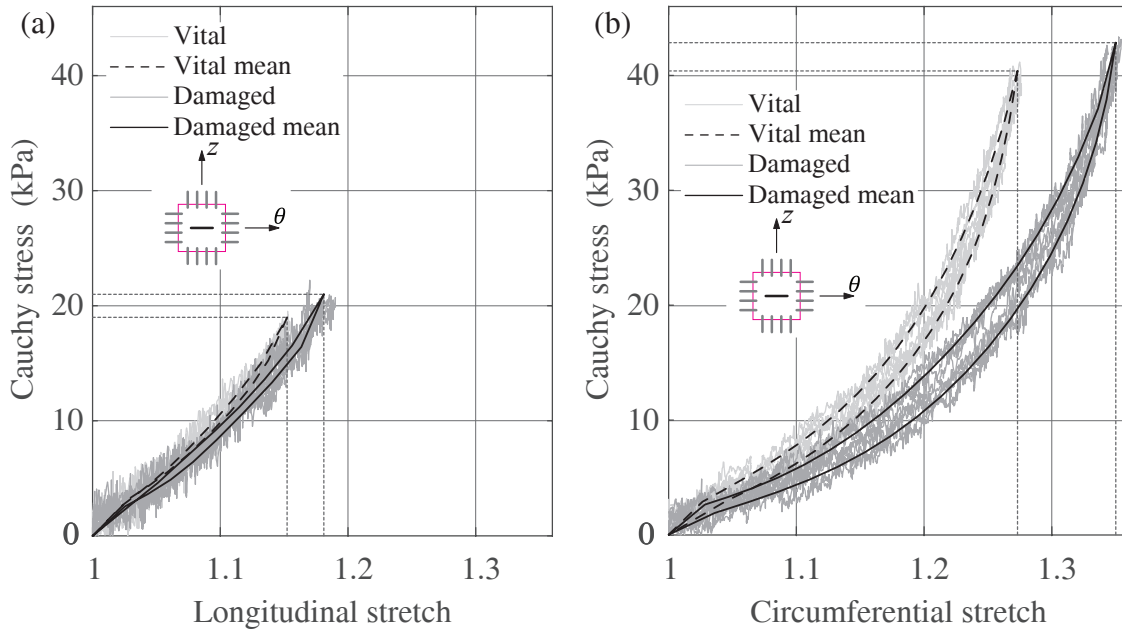

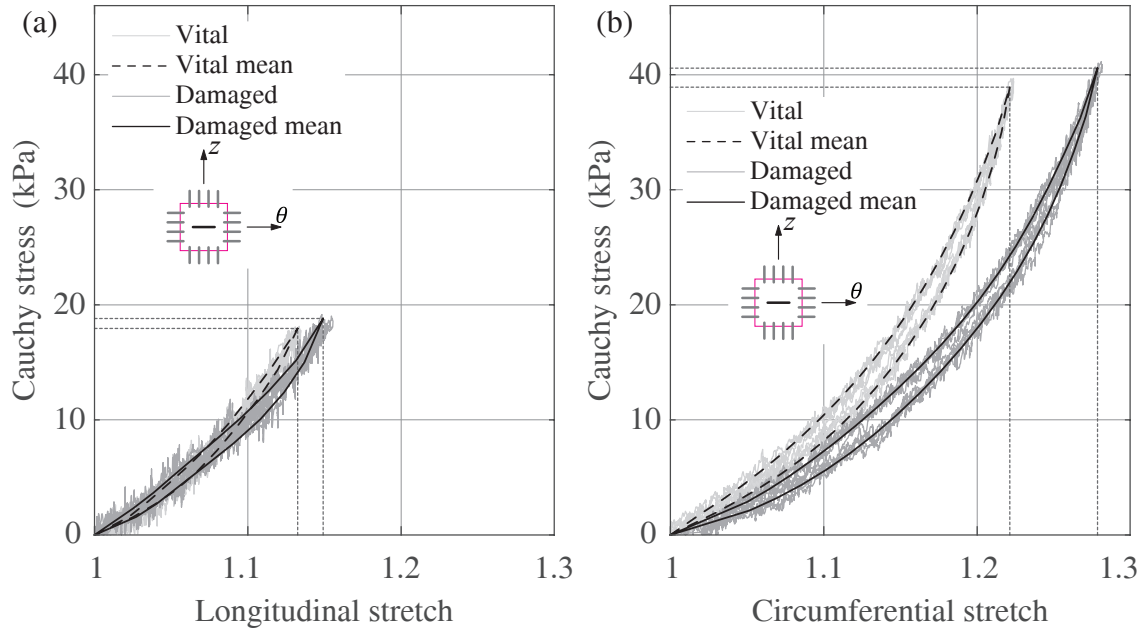Figure 3.7   Representative Cauchy stress vs. stretch plots of sample DVII with the stamp indenting at the angle $\iota = 90°$ and with the force $F_{\mathrm{ind}} = 1\,\mathrm{N}$. The mechanical response under physiological load of the vital and the damaged sample is indicated with the dashed and the solid black curve, respectively. Mechanical response (a) in the longitudinal and (b) in the circumferential direction.

Figure 3.8 compares the mechanical vascular damage of the RCA samples tested with the same stamp orientation but with a different indentation force. Figure 3.8 compares sample AII and sample BIV, where the stamp was indented at the angle $\iota = 0°$. The stamp was indented with the force $F_{\mathrm{ind}} = 2\,\mathrm{N}$ into sample AII and with the force $F_{\mathrm{ind}} = 1\,\mathrm{N}$ into sample BIV. In Figure 3.8(a) the mechanical response in the longitudinal direction is shown. The difference in the maximum stretches of sample AII exhibits a softening of $\Delta\lambda_z = 0.014$ (gain: $11.5\,\%$) and sample BIV shows a softening of $\Delta\lambda_z = 0.007$ (gain: $4.9\,\%$). The softening in the longitudinal direction is twice as high for twice the force. In Figure 3.8(b) the mechanical response in the circumferential direction is displayed, where the difference in the maximum stretches of sample AII shows a softening of $\Delta\lambda_\theta = 0.129$ (gain: $51.8\,\%$) and sample BIV shows a softening of $\Delta\lambda_\theta = 0.05$ (gain: $19.6\,\%$). With the stamp indenting at the angle $\iota = 0°$ the higher stamp force of $2\,\mathrm{N}$ softens the tissue more severe than the stamp force of $1\,\mathrm{N}$.

Figure 3.8　　Representative Cauchy stress vs. stretch plots, which compare the mechanical vascular damage due to different indentation forces, with the stamp indenting at the angle $\iota = 0°$. The stamp was indented into sample AII with the force $F_{\mathrm{ind}} = 2\,\mathrm{N}$ and into sample BIV with the force $F_{\mathrm{ind}} = 1\,\mathrm{N}$. The mechanical response under physiological load of the vital sample and the damaged sample is indicated with the dashed and the solid curve, respectively. Mechanical response (a) in the longitudinal and (b) in the circumferential direction.

Figure 3.9 compares the mechanical vascular damage of the RCA samples, tested with the same stamp orientation, but with a different indentation force. Figure 3.9 compares sample CVI and sample DVII, where the stamp was indented at the angle $\iota = 90°$ and the force $F_{ind} = 2\,N$ into sample CVI and with the force $F_{ind} = 1\,N$ into sample DVII. In Figure 3.9(a) the mechanical response in the longitudinal direction is shown. The difference in the maximum stretches of sample CVI exhibits a softening of $\Delta\lambda_z = 0.027$ (gain: 18.9 %) and sample BIV shows a softening of $\Delta\lambda_z = 0.017$ (gain: 12.5 %). The softening of the tissue of the different stamp indentation force in the longitudinal direction is more pronounced for the higher force. In Figure 3.9(b) the mechanical response in the circumferential direction is displayed, with the difference in the maximum stretches of sample CVI showing a softening of $\Delta\lambda_\theta = 0.072$ (gain: 28.2 %) and of sample BIV showing a softening of $\Delta\lambda_\theta = 0.057$ (gain: 25.8 %). It ensures that if the stamp is indenting at the angle $\iota = 90°$, the higher stamp force of $2\,N$ softens the tissue more significant than the stamp force of $1\,N$.
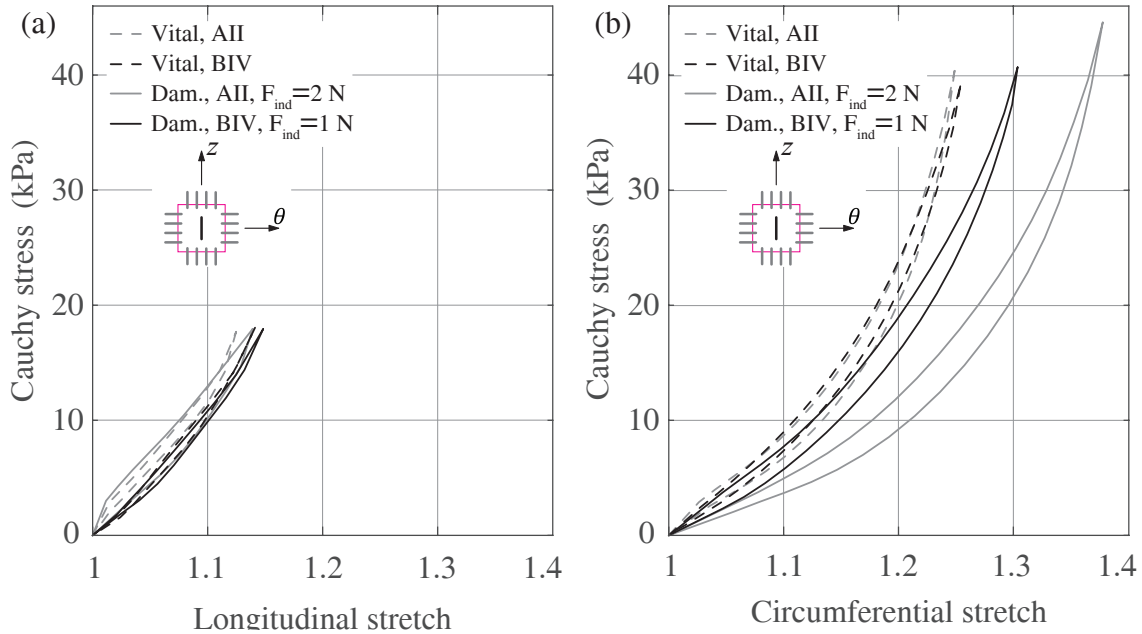

Figure 3.9   Representative Cauchy stress vs. stretch plots, which compare the mechanical vascular damage due to different indentation forces, with the stamp indenting at the angle $\iota = 90°$. The stamp was indented into sample CVI with the force $F_{ind} = 2\,N$ and into sample DVII with the force $F_{ind} = 1\,N$. The mechanical response under physiological load of the vital sample and the damaged sample is indicated with the dashed and the solid curve, respectively. Mechanical response (a) in the longitudinal and (b) in the circumferential direction.

Figure 3.10 compares the mechanical vascular damage of the coronary artery samples, tested with the same stamp indentation force but, with a different stamp orientation. Figure 3.10 compares sample AII and sample CVI, where the stamp was indented with the force $F_{\text{ind}} = 2\,\text{N}$ at the angle $\iota = 0°$ into sample AII and at the angle $\iota = 90°$ into sample CVI. In Figure 3.10(a) the mechanical response in the longitudinal direction is shown. The difference in the maximum stretches of sample AII exhibits a softening of $\Delta\lambda_z = 0.014$ (gain: 11.5 %) and sample CVI shows a softening of $\Delta\lambda_z = 0.027$ (gain: 18.9 %). The softening of sample CVI is more pronounced than for sample AII. In Figure 3.10(b) the mechanical response in the circumferential direction is displayed, where the difference in the maximum stretches of sample AII shows a softening of $\Delta\lambda_\theta = 0.129$ (gain: 51.8 %) and for sample CVI a softening of is $\Delta\lambda_\theta = 0.072$ (gain: 28.2 %). This states that the force 2 N and the stamp indentation at the angle $\iota = 90°$ softens the tissue more significant than the stamp indentation at the angle $\iota = 0°$.
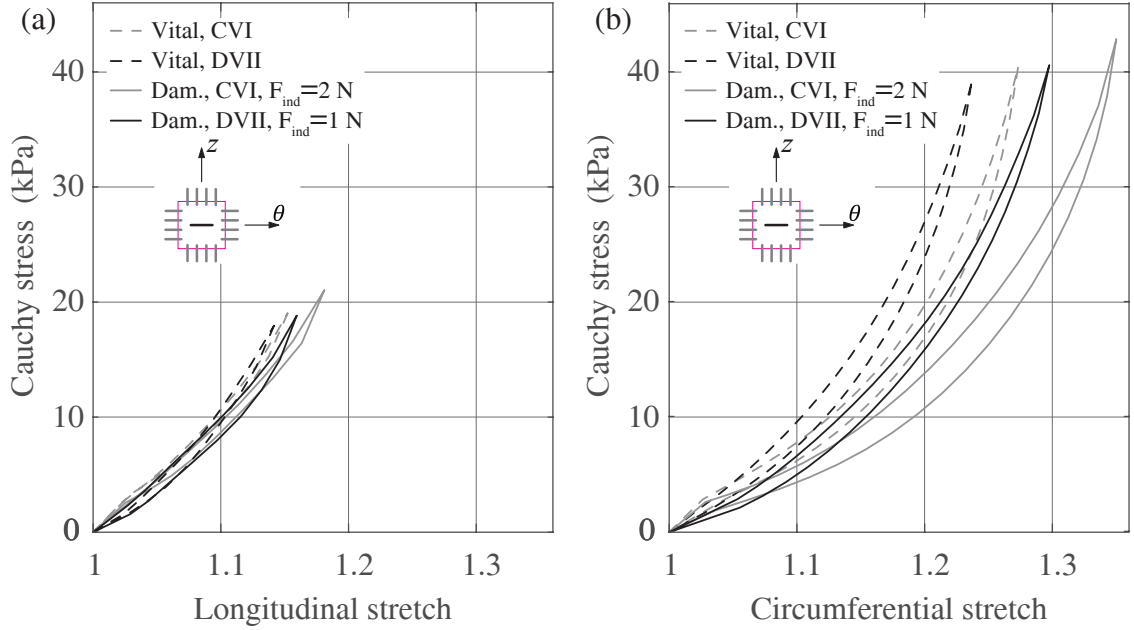

Figure 3.10   Representative Cauchy stress vs. stretch plots, which compare the mechanical vascular damage due to different stamp orientations, with the stamp indenting with the force $F_{\text{ind}} = 2\,\text{N}$. The stamp orientation of sample AII is at the angle $\iota = 0°$ and of sample CVI at the angle $\iota = 90°$. The mechanical response under physiological load of the vital sample and the damaged sample is indicated with the dashed and the solid curve, respectively. Mechanical response (a) in the longitudinal direction and (b) in the circumferential direction.

Figure 3.11 compares the mechanical vascular damage of the coronary artery samples tested with the same stamp indentation force but with a different stamp orientation. Figure 3.11 compares sample BIV and DVII, where the stamp was indented with the force $F_{\mathrm{ind}} = 1\,\mathrm{N}$ at the angle $\iota = 0°$ into sample BIV and at the angle $\iota = 90°$ into sample DVII. In Figure 3.11(a) the mechanical response in the longitudinal direction is shown. The difference in the maximum stretches of sample BIV exhibits a softening of $\Delta\lambda_z = 0.007$ (gain: $4.9\,\%$) and for sample DVII a softening of $\Delta\lambda_z = 0.017$ (gain: $12.5\,\%$). The softening of DVII is significantly softer compared to sample BIV. Figure 3.11(b) displays the mechanical response in the circumferential direction, where the difference in the maximum stretches of sample BIV shows a softening of $\Delta\lambda_\theta = 0.05$ (gain: $19.6\,\%$) and for sample DVII a softening of $\Delta\lambda_\theta = 0.057$ (gain: $25.8\,\%$). The direction of the stamp indenting with the force $F_{\mathrm{ind}} = 1\,\mathrm{N}$ shows no difference in respect of softening of the tissue.
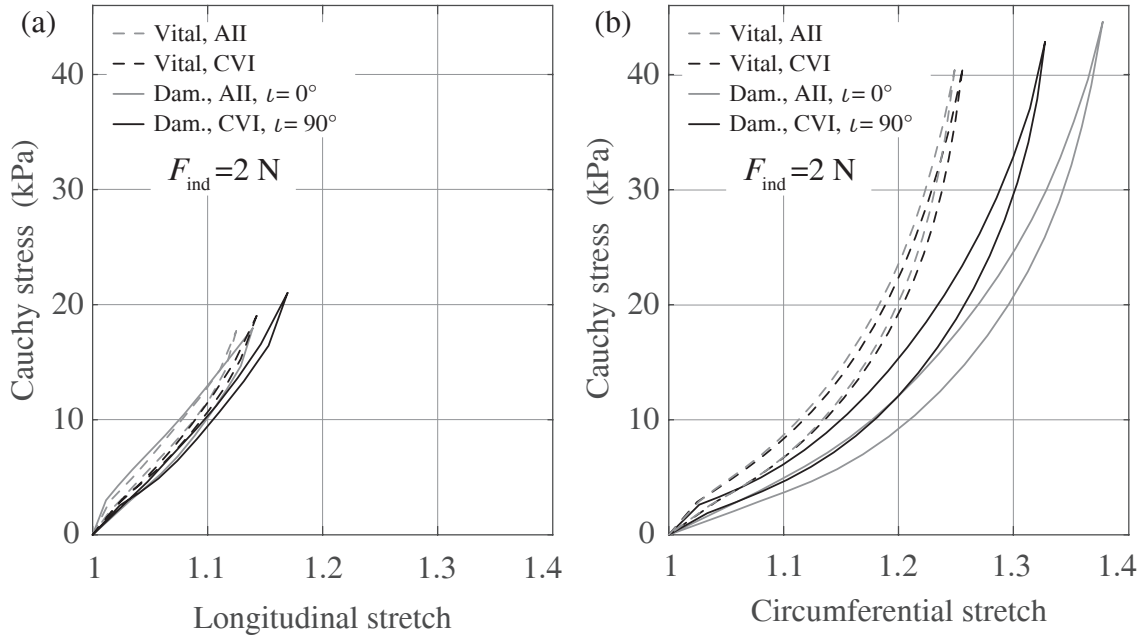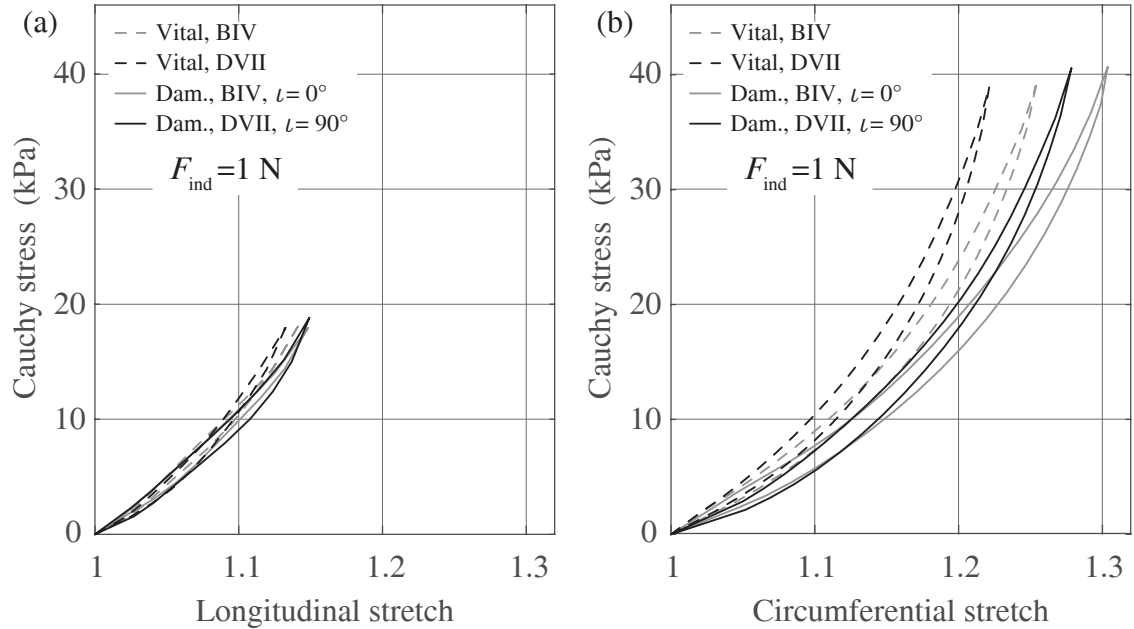

Figure 3.11   Representative Cauchy stress vs. stretch plots, which compare the mechanical vascular damage due to different stamp orientations, with the stamp indenting with the force $F_{\mathrm{ind}} = 1\,\mathrm{N}$. The stamp orientation of sample BIV is at the angle $\iota = 0°$ and of sample DVII at the angle $\iota = 90°$. The mechanical response under physiological load of the vital sample and the damaged sample is indicated with the dashed and the solid curve, respectively. Mechanical response (a) in the longitudinal direction and (b) in the circumferential direction.

3.3.1 Tissue Softening Overview

Figure 3.12 shows the mean of the maximal measured stretch (a) and stress (b) of testing series A where the stamp was indented at the angle $\iota = 0°$ with the force $F_{\mathrm{ind}} = 2\,\mathrm{N}$. It was observed that both tested samples of testing series A showed similar results. Figure 3.12(a) shows a difference in the maximum stretches of testing series A of $\Delta\lambda_z = 0.018\,(\text{gain: }13.0\,\%)$ and in the circumferential direction a softening of $\Delta\lambda_\theta = 0.118\,(\text{gain: }50.0\,\%)$ occurred. Further, for the longitudinal direction no change of the stress is observed, but in the circumferential direction a rise of the stress of $\Delta\sigma_{\theta\theta} = 5.1\,\mathrm{kPa}$ occurred. This is displayed in Figure 3.12(b).

Figure 3.12 Mean (a) stress and (b) stretch bar plot of testing series A with the stamp indenting at the angle $\iota = 0°$ with the force $F_{\mathrm{ind}} = 2\,\mathrm{N}$. The green bars show the vital state and the red bars show the damaged state of the sample.

Figure 3.13 shows the mean of the maximal measured stretch (a) and stress (b) of testing series B, where the stamp was indented at the angle $\iota = 0°$ with the force $F_{\mathrm{ind}} = 1\,\mathrm{N}$. It was observed that both tested samples of testing series B showed similar results. The difference in the maximum stretches of testing series B in the longitudinal direction shows a softening of $\Delta\lambda_z = 0.009\,(\text{gain: }7.5\,\%)$ and in the circumferential direction a softening of $\Delta\lambda_\theta = 0.053\,(\text{gain: }25.7\,\%)$ is recorded. This is displayed in Figure 3.13(a). Figure 3.13(b) shows that the stresses in the longitudinal direction do not change due to the non-significant softening in this direction. The stress in the circumferential direction shows a rise of $\Delta\sigma_{\theta\theta} = 3.3\,\mathrm{kPa}$. This states that the sample gets softened in the circumferential direction.
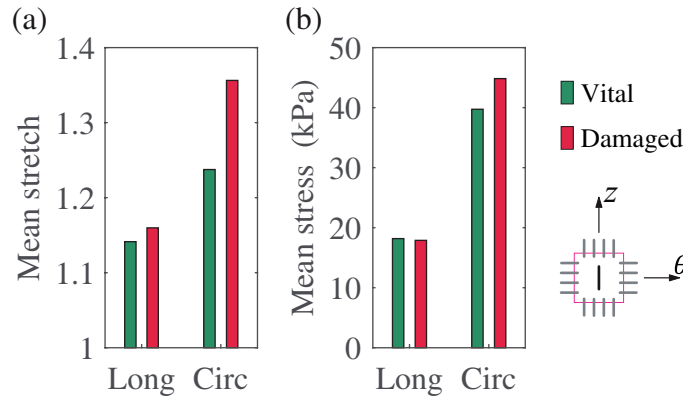
Figure 3.13 Mean (a) stress and (b) stretch bar plot of testing series B with the stamp indenting at the angle $\iota = 0°$ with the force $F_{\text{ind}} = 1\,\text{N}$. The green bars show the vital state and the red bars show the damaged state of the sample.

Figure 3.14 shows the mean of the maximal measured stretch (a) and stress (b) of testing series C, where the stamp was indented in the circumferential direction at the angle $\iota = 90°$ with the force $F_{\text{ind}} = 2\,\text{N}$. It was observed that both tested samples of testing series B showed similar results. A softening of $\Delta\lambda_z = 0.028$ (gain: 20.2 %) occurred in the longitudinal direction, shown in Figure 3.14(a), and in the circumferential direction a softening of $\Delta\lambda_\theta = 0.085$ (gain: 38.5 %) occurred. Figure 3.14(b) displays that the stress in the longitudinal direction is rising by $\Delta\sigma_{zz} = 1.3\,\text{kPa}$ and in the circumferential direction a rise by $\Delta\sigma_{\theta\theta} = 3.6\,\text{kPa}$ occurred.

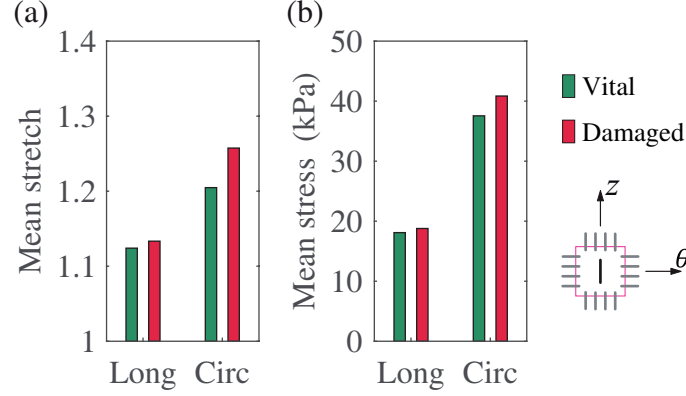Figure 3.14 Mean (a) stress and (b) stretch bar plot of testing series C with the stamp indenting at the angle $\iota = 90°$ with the force $F_{\text{ind}} = 2\,\text{N}$. The green bars show the vital state and the red bars show the damaged state of the sample.

Figure 3.15 shows the mean of the maximal measured stretch (a) and stress (b) of testing series D, where the stamp was indented in the circumferential direction at the angle $\iota = 90°$ with the force $F_{\mathrm{ind}} = 1\,\mathrm{N}$. It was observed that both tested samples of testing series B showed similar results. Figure 3.15(a) shows a softening in the longitudinal direction by the difference in the maximum stretches of $\Delta\lambda_z = 0.018\,(\text{gain: } 12.2\,\%)$ and in the circumferential direction a difference of $\Delta\lambda_\theta = 0.066\,(\text{gain: } 29.6\,\%)$ is observed. Figure 3.15(b) shows that there is no change of the stress in the longitudinal direction, and in the circumferential direction a rise by $\Delta\sigma_{\theta\theta} = 2.6\,\mathrm{kPa}$ occurred.
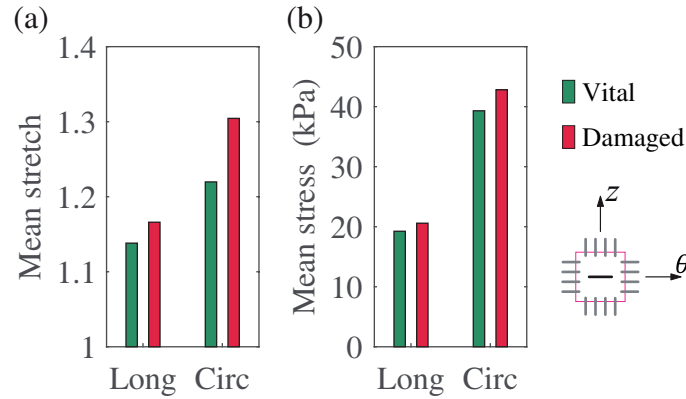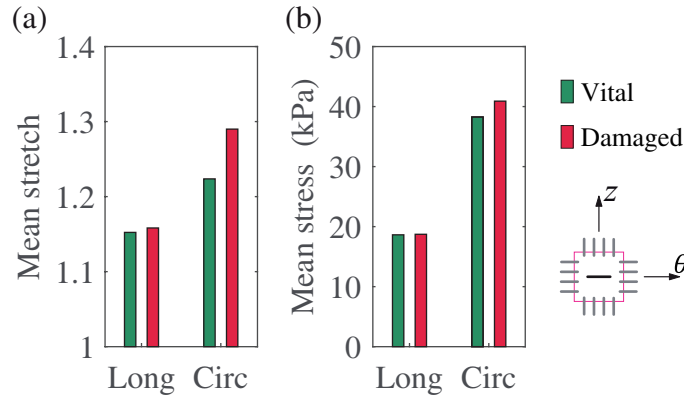

Figure 3.15   Mean (a) stress and (b) stretch bar plot of testing series D with the stamp indenting at the angle $\iota = 90°$ with the force $F_{\mathrm{ind}} = 1\,\mathrm{N}$. The green bars show the vital state and the red bars show the damaged state of the sample.

3.4 Microstructural Analysis

For the analysis of the collagen fiber orientation of five porcine RCA samples, i.e. one native sample and four damaged samples, were investigated, listed in Table 2.2 with the stamp indentation parameters. The 3D-surface scans in the Figures 3.16 - 3.19 show the cross section of the sample through the middle of the indentation, as shown in the schematic cross section in Figure 2.19, where a difference in shape of the lesion can be detected. All samples show a homogeneous compression at the center of the lesion.

Figure 3.16 shows the 3D-surface scan of one half of the damaged sample LI. In the middle of the sample the lesion is displayed and it shows a large deformation, but for the stamp indenting at the angle $\iota = 0°$ and the indentation force of $F_{\text{ind}} = 1\,\text{N}$ no rupture or delamination occurred. The lesion sides gradually rise at a very flat angle, consequently the distance k_{max} is large. The compression at the deepest point of the indentation is $\lambda_r^{\min} = 0.11$.

Figure 3.16   Half isometric 3D-surface scan of the injured sample LI. The stamp was indented in the circumferential direction at the angle $\iota = 0°$, with the force $F_{\text{ind}} = 1\,\text{N}$. $\lambda_r^{\min}$: compression in the center of the lesion, k_{max}: distance between the indentation and the virgin part.

Figure 3.17 shows the 3D-surface scan of one half of the damaged sample LII. For the stamp indented at the angle $\iota = 0°$ and the force of $F_{\mathrm{ind}} = 2\,\mathrm{N}$, severe delamination occurred at the corners of the stamp and, therefore, the sample is heaped up slightly. This results due to force singularities at the corners of the stamp. The flanks perpendicular to the lesion rise at a very flat angle, which results in a higher distance k_{max} from the center of the lesion to the virgin part. The compression at the deepest point of the indentation is increasing with the higher indentation force to a value of $\lambda_r^{\mathrm{min}} = 0.09$.

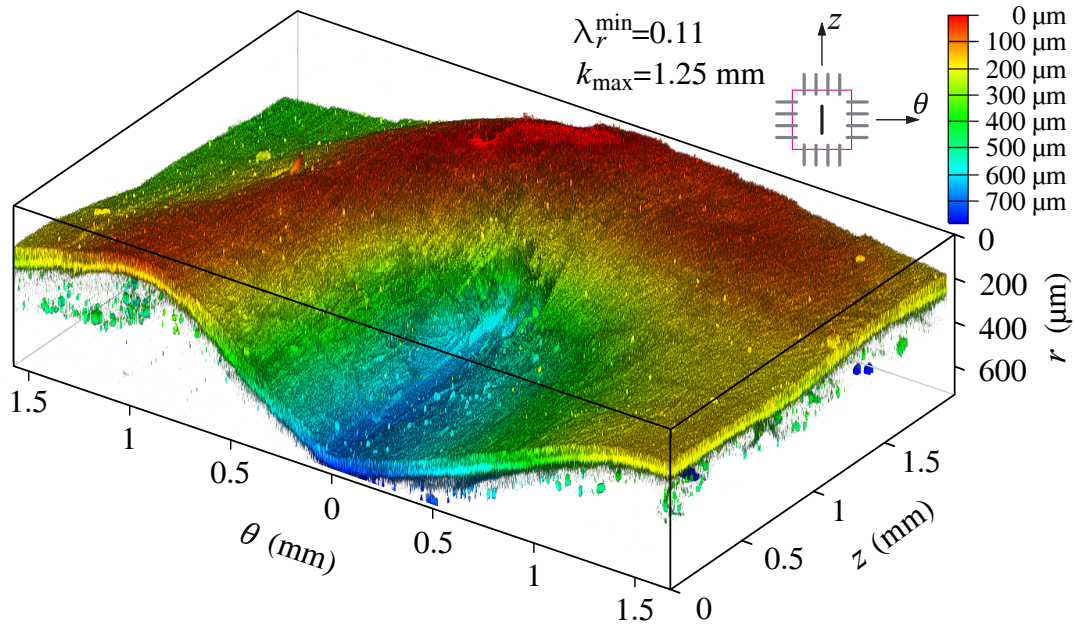Figure 3.17   Half isometric 3D-surface scan of the injured sample LII. The stamp was indented in the circumferential direction at the angle $\iota = 0°$, with the force $F_{\mathrm{ind}} = 2\,\mathrm{N}$. λ_r^{min}: compression in the center of the lesion, k_{max}: distance between the indentation and the virgin part.

Figure 3.18 shows the 3D-surface scan of one half of the damaged sample CI. The sample was deformed heavily with the lesion visible in the middle of the figure and it shows that no rupture or delamination occurred due to the stamp indenting at the angle $\iota = 0°$ and the force of $F_{\text{ind}} = 1\,\text{N}$. The scan reveals that at the corners of the stamp the sample is heaped up slightly and that the flanks of the lesion are rather steep. Hence, the distance k_{max} is small, i.e. the virgin part is close to the center of the lesion. The compression at the deepest point of the indentation is increasing when the stamp is oriented in the circumferential direction in comparison with the longitudinal stamp orientation. The sample experienced a compression of $\lambda_r^{\text{min}} = 0.09$.
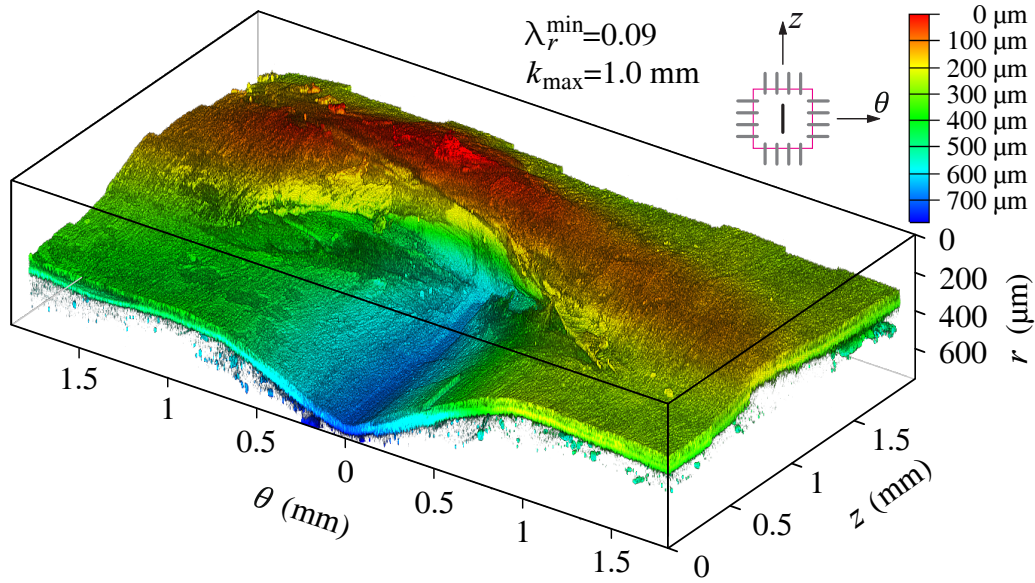

Figure 3.18   Half isometric 3D-surface scan of the injured sample CI. The stamp was indented in the circumferential direction at the angle $\iota = 90°$, with the force $F_{\text{ind}} = 1\,\text{N}$. λ_r^{min}: compression in the center of the lesion, k_{max}: distance between the indentation and the virgin part.

Figure 3.19 shows the 3D-surface scan of one half of the damaged sample CII. The sample was deformed heavily with the lesion visible in the middle of the figure and it shows that delamination occurred parallel to the stamp which was indented at the angle $\iota = 90°$ and the force of $F_{ind} = 2\,N$. At the edges of the stamp the sample is heaped up and shows severe delamination. Figure 3.20 shows the sample cross section, where the delamination is clearly visible. The sides of the lesion rise at a steep angle from the lesion. Consequently, the virgin part is close to the center of the lesion. The compression at the deepest point of the indentation is increasing with the higher indentation force to a value of $\lambda_r^{min} = 0.07$.
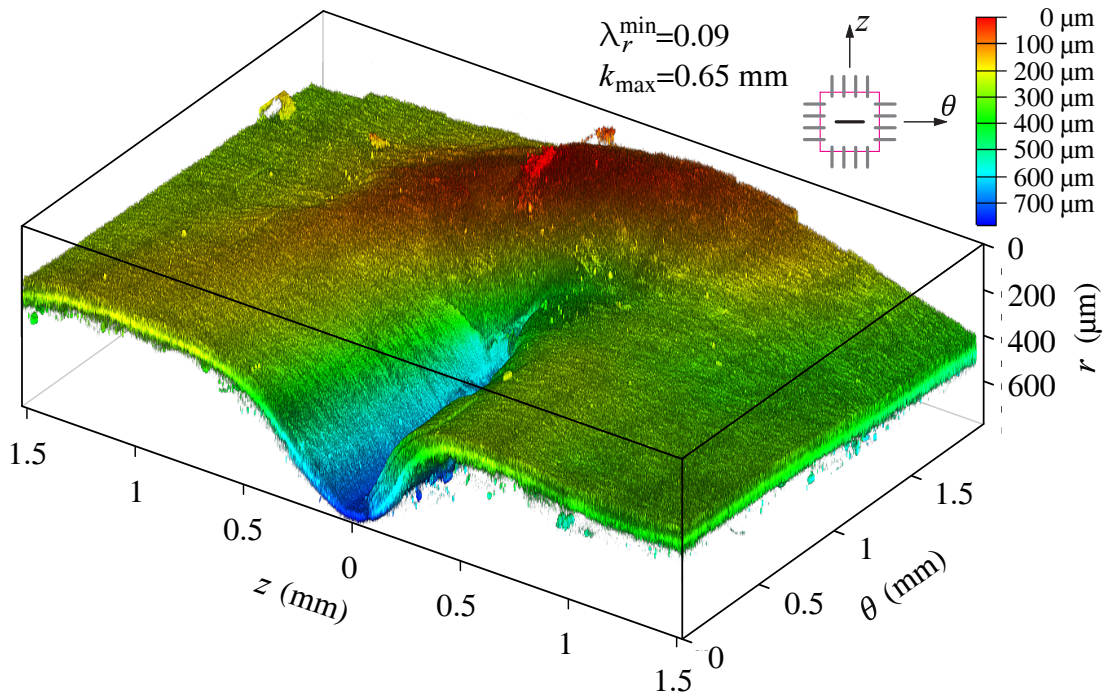

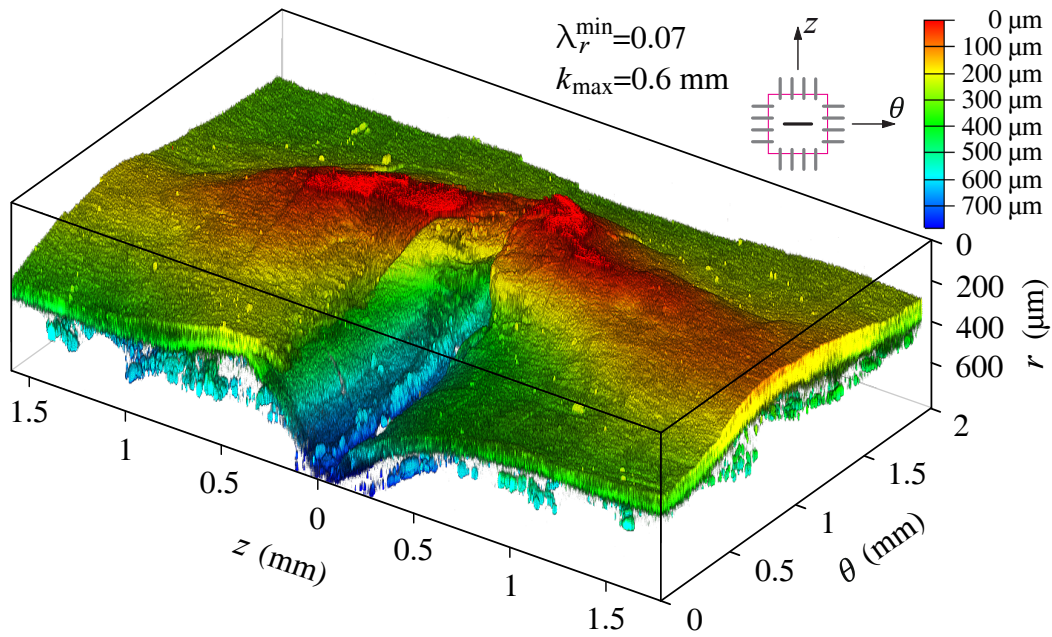Figure 3.19   Half isometric 3D-surface scan of the injured sample CII. The stamp was indented in the circumferential direction at the angle $\iota = 90°$, with the force $F_{ind} = 2\,N$. λ_r^{min}: compression in the center of the lesion, k_{max}: distance between the indentation and the virgin part.
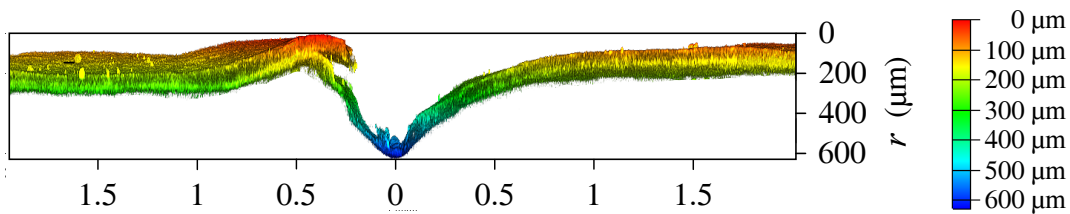

Figure 3.20   Cross section of the of the sample CII, which shows the delamination parallel to the indentation.

Within the aortic wall of the tested RCA samples, the distinct layers could be identified. Figure 3.21(a) shows SHG images of a representative native RCA sample. The three images display in-plane sections of the media and the adventitia. The media (M) in Figure 3.21(a) shows thin collagen fibers, which are oriented towards the circumferential direction. The adventita is divided into two parts: the inner adventitia (IA) with concentric thin wavy fibers and the outer adventitia (OA) with thicker wavy fiber bundles, which are more oriented towards the longitudinal direction. Furthermore, out-of-plane scans show the fiber orientation through the thickness of the sample, in the longitudinal and the circumferential direction. The intensity plot shown in Figure 3.21(b) displays the collagen fiber orientation and dispersion through the RCA wall, where dark red depicts no dispersion and blue relates to no fibers under this angle. The fiber orientation of the intima (I) and the basal lamina (BL) which is the subendothelial layer, can be seen at the top of the intensity plot, showing a strong dispersion around the circumferential direction. In the media it shows a fiber orientation in the circumferential direction with rather low dispersion. The external elastic lamina (EL) appears between the media and the adventitia. The fibers in the inner adventitia with an orientation in the circumferential direction similar to the fiber orientation in the media, which was found in a previous study by Chen and Kassab [7]. In the outer adventitia, the fibers are oriented towards the longitudinal direction.

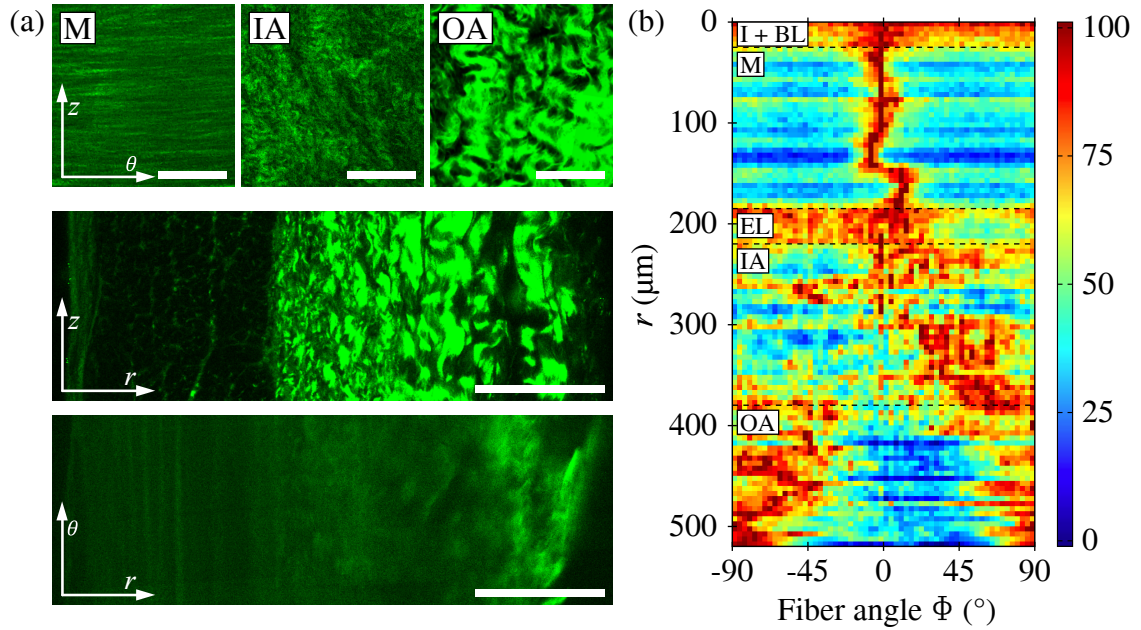Figure 3.21 Structure of a representative native RCA sample: (a) SHG images showing the in-plane section of the media (M), the inner (IA) and outer adventitia (OA), while on the bottom an out-of-plane scan through the thickness is displayed. Scale bar, $100\,\mu m$; (b) intensity plot showing collagen fiber orientation and dispersion through the depth (radial direction) of the native RCA sample. ϕ: fiber angle.

Figure 3.22(a) shows SHG images and the intensity plot of the virgin part of sample LI at the distance k_{max} from the center of the lesion. The SHG images and the intensity plot despite the media and the two parts of the adventitia, where the image of the media (M) and the inner adventitia (IA) show that the fibers are oriented in the circumferential direction. The image of the outer adventitia (OA) displays the fiber orientation towards the longitudinal direction. The image through the thickness is an out-of-plane scan and displays the media on the left followed by the adventitia. It confirms the fiber orientation, which can be seen in the SHG images. The SHG images and the intensity plot in Figure 3.22(b) show the damaged section of the sample at the distance $k_{\mathrm{max}}/3$ from the center of the sample. The fiber in the media (M) and the inner adventitia (IA) are oriented in the circumferential direction. The image of the outer adventitia (OA) shows that the collagen fibers are straightened out and oriented more towards the longitudinal direction. The out-of-plane scan displays the media on the left, followed by the adventitia with straightened out collagen fibers.

Figure 3.22   In-plane and out-of plane SHG images and intensity plots showing the collagen fiber orientation and dispersion through the depth of the RCA sample LI with the layers media (M), the inner (IA) and outer adventitia (OA): (a) layered structure of the virgin part; (b) layered structure of the damaged part. Scale bar, $100\,\mu\mathrm{m}$. ϕ: fiber angle.

Figure 3.23(a) shows SHG images and the intensity plot of the virgin part of sample LII at the distance k_{max} from the center of the lesion. The fibers in the media (M) and the inner adventitia (IA) are oriented more towards the circumferential direction with low dispersion. The image of the outer adventitia (OA) displays the thick fiber bundle structure, where the fibers are more oriented towards the longitudinal direction. The out-of-plane scan displays the media on the left, followed by the two parts of the adventitia. The SHG images and the intensity plot in Figure 3.23(b) show the damaged section of the sample at the distance $k_{max}/3$ from the center of the lesion. The thin fiber in the media (M) and the inner adventitia (IA) are oriented more towards the circumferential direction. In the outer adventitia (OA), the fibers are straightened out and are oriented towards the longitudinal direction. The image through the thickness is an out-of-plane scan, displaying the media on the left, followed by the adventitia with straightened out collagen fibers.
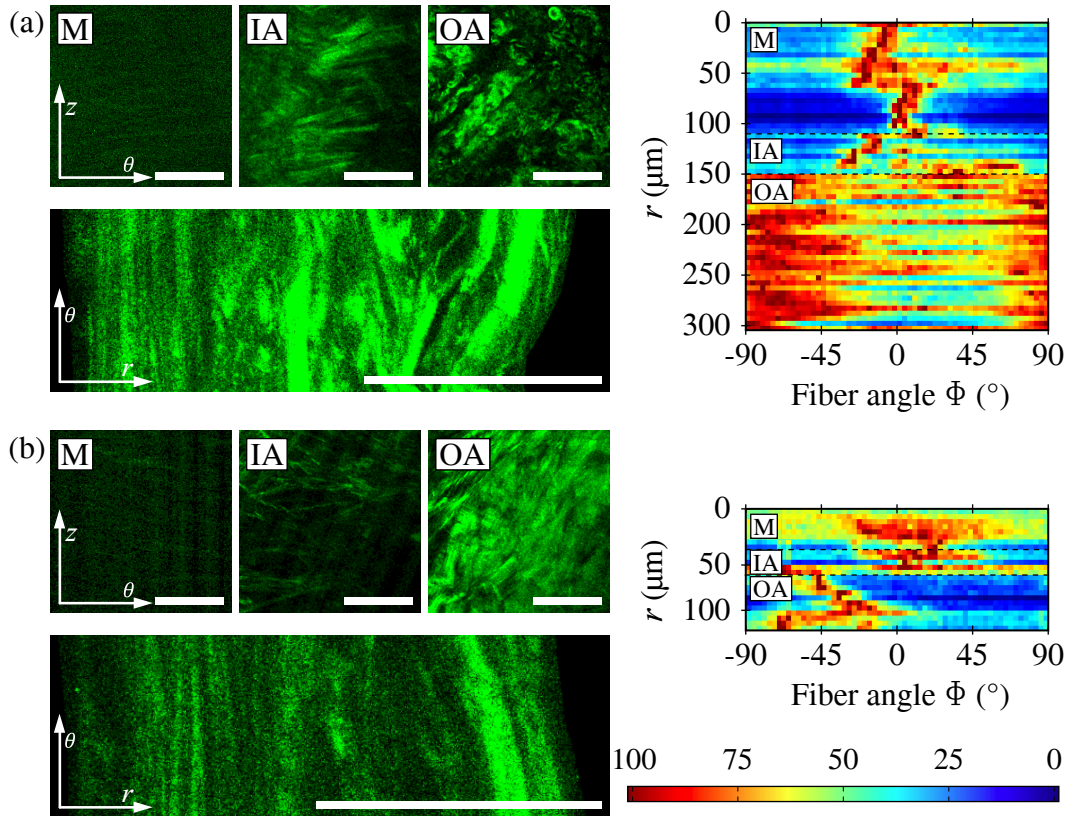

Figure 3.23   In-plane and out-of plane SHG images and intensity plots showing the collagen fiber orientation and dispersion through the depth of the RCA sample LII with the layers media (M), the inner (IA) and outer adventitia (OA): (a) layered structure of the virgin part; (b) layered structure of the damaged part. Scale bar, $100\,\mu m$. ϕ: fiber angle.

Figure 3.24(a) shows SHG images and the intensity plot of the virgin part of sample CI at the distance k_{max} from the lesion. The SHG images and the intensity plots show the media and the two parts of the adventitia, where the image of the media (M) reveals that the fibers are oriented in the circumferential direction. The fibers in the inner adventitia (IA) show a high distortion but are more oriented towards the circumferential direction. The fibers in the outer adventitia (OA) appear as rather straight thick collagen struts, which are more oriented towards the longitudinal direction. The out-of-plane scan displays the media on the left, followed by the inner adventitia and the outer adventitia with the wavy structure. The SHG images and the intensity plot in Figure 3.24(b) show the damaged section of the sample close to the lesion at the distance $k_{max}/3$ from the center of the sample. The fiber orientation of the sample differ only slightly from the virgin part, with a decreasing dispersion. The out-of-plane scan displays the media on the left, followed by the two parts of the adventitia.
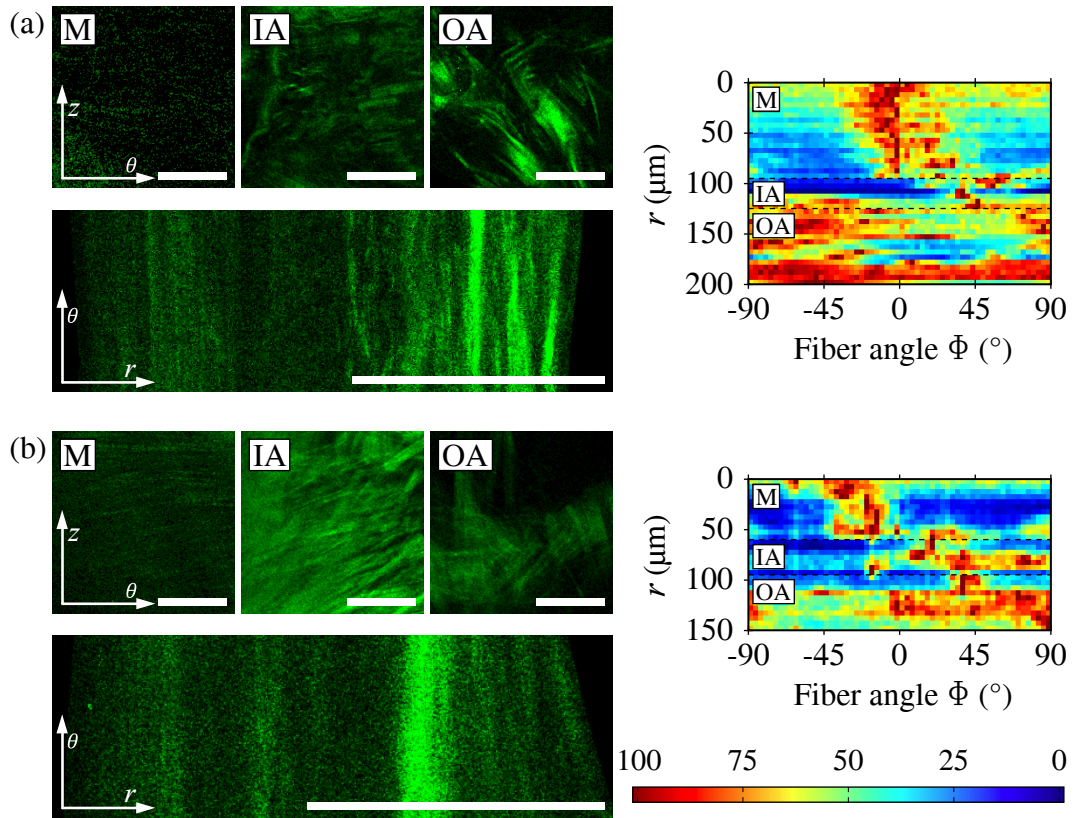

Figure 3.24   In-plane and out-of plane SHG images and intensity plots showing the collagen fiber orientation and dispersion through the depth of the RCA sample CI with the layers media (M), the inner (IA) and outer adventitia (OA): (a) layered structure of the virgin part; (b) layered structure of the damaged part. Scale bar, $100\,\mu m$. ϕ: fiber angle.

Figure 3.25(a) shows SHG images and the intensity plot of the virgin part of sample CII at the distance k_{max} from the lesion. The fibers in the media (M) are oriented towards the circumferential direction. In the inner adventitia (IA) the fibers are oriented in the circumferential direction and slowly fulfill an orientation change towards the longitudinal direction. The rather straight thick collagen struts of the outer adventitia (OA) are oriented in the longitudinal direction. The out-of-plane scan and displays the media on the left, followed by the two parts of the adventitia. The SHG images and the intensity plot in Figure 3.25(b) show the damaged section of the sample at the distance $k_{max}/3$ from the center of the lesion. The fiber orientation of the media (M) and the inner adventitia (IA) is the same as in the virgin part, but the fibers are less dispersed. The fibers in the outer adventitia (OA) are more oriented towards the longitudinal direction. The out-of-plane scan displays the media on the left, where no fibers are detected, followed by the two parts of the adventitia, where the fibers are straightened out.
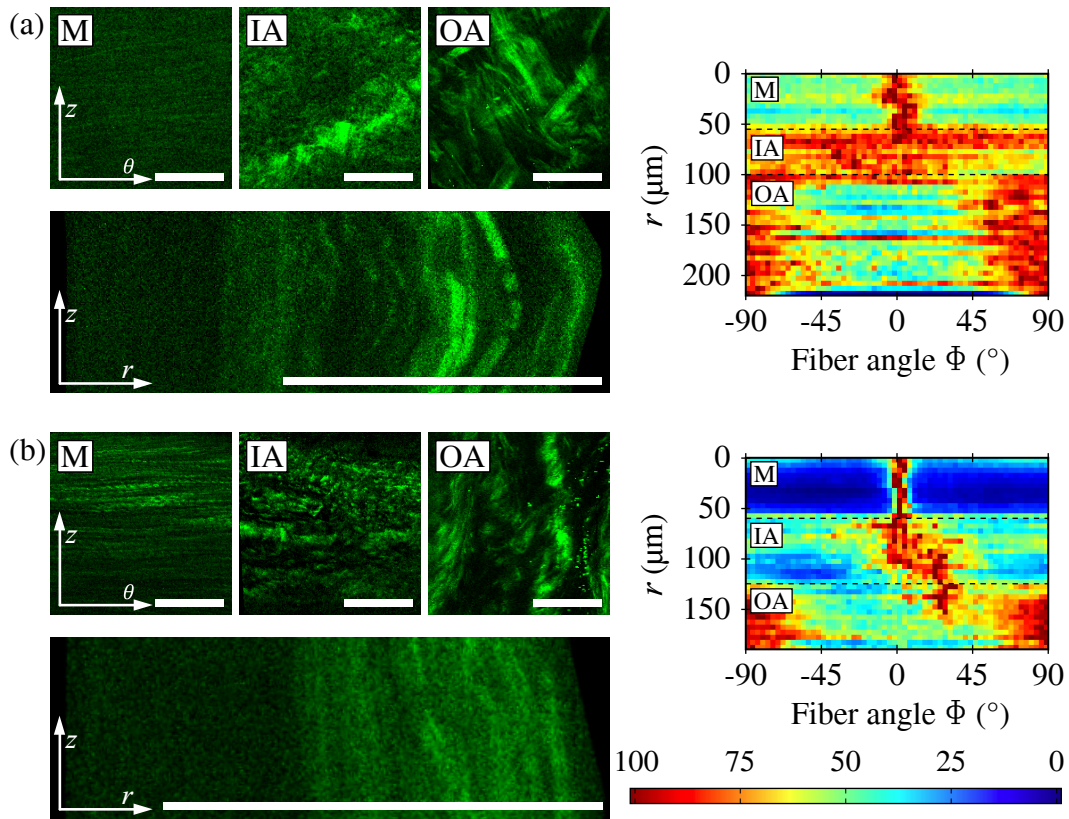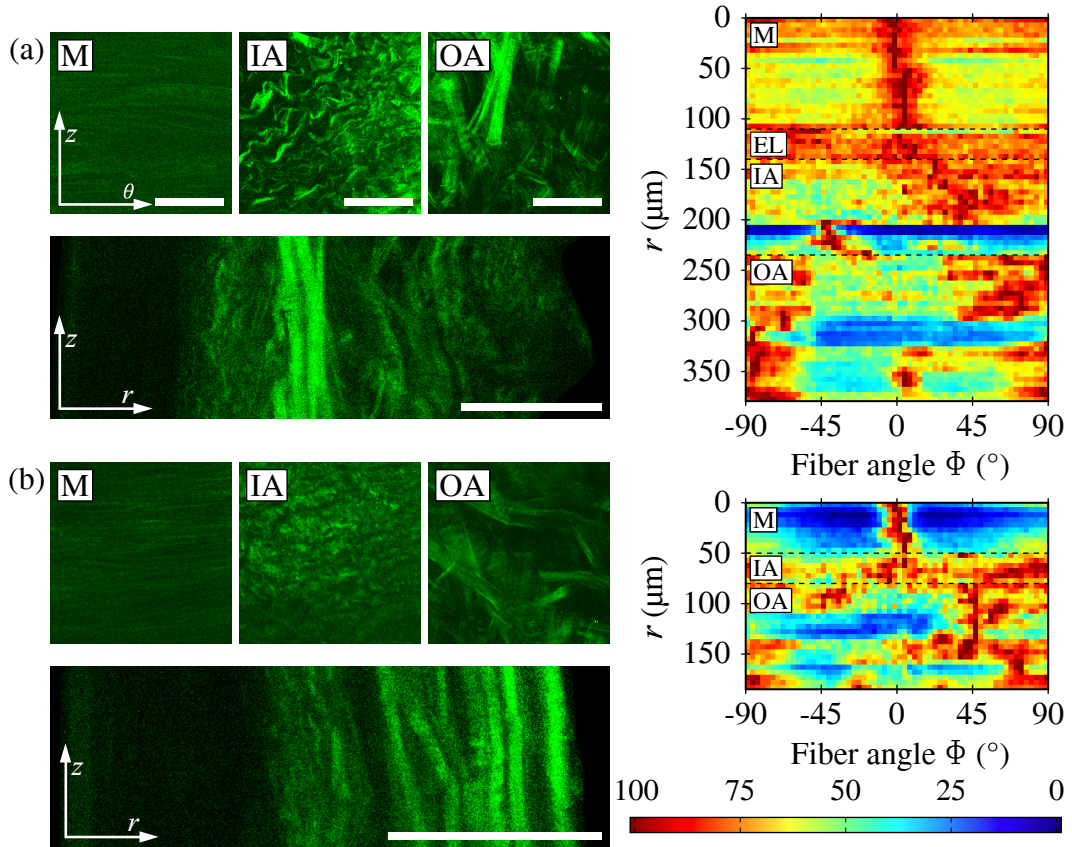

Figure 3.25 In-plane and out-of plane SHG images and intensity plots showing the collagen fiber orientation and dispersion through the depth of the RCA sample CII with the layers media (M), the inner (IA) and outer adventitia (OA): (a) layered structure of the virgin part; (b) layered structure of the damaged part. Scale bar, $100\,\mu m$. ϕ: fiber angle.

Figure 3.26 shows the mosaic out-of-plane SHG scans in the longitudinal and the circum-
ferential direction of the native sample under physiological load. Figure 3.26(a) shows
the scan in the longitudinal direction, where no fibers are visible in the media (M). In the
adventitia the typical wavy structure of the collagen fiber bundles is visible because the
fibers are oriented mostly in the longitudinal direction. In the inner adventitia (IA) the
fibers are thinner and in the outer adventitia (OA) the fibers become thicker fiber bundles.
Figure 3.26(b) shows the out-of-plane scan in the circumferential direction, where collagen
fibers are visible in the media (M) because they are oriented in the circumferential direc-
tion. In the adventitia the structure is recognizable, but no clear fiber bundle structure is
identifiable, because the fibers are cut perpendicular to their orientation.

(a)

(b)
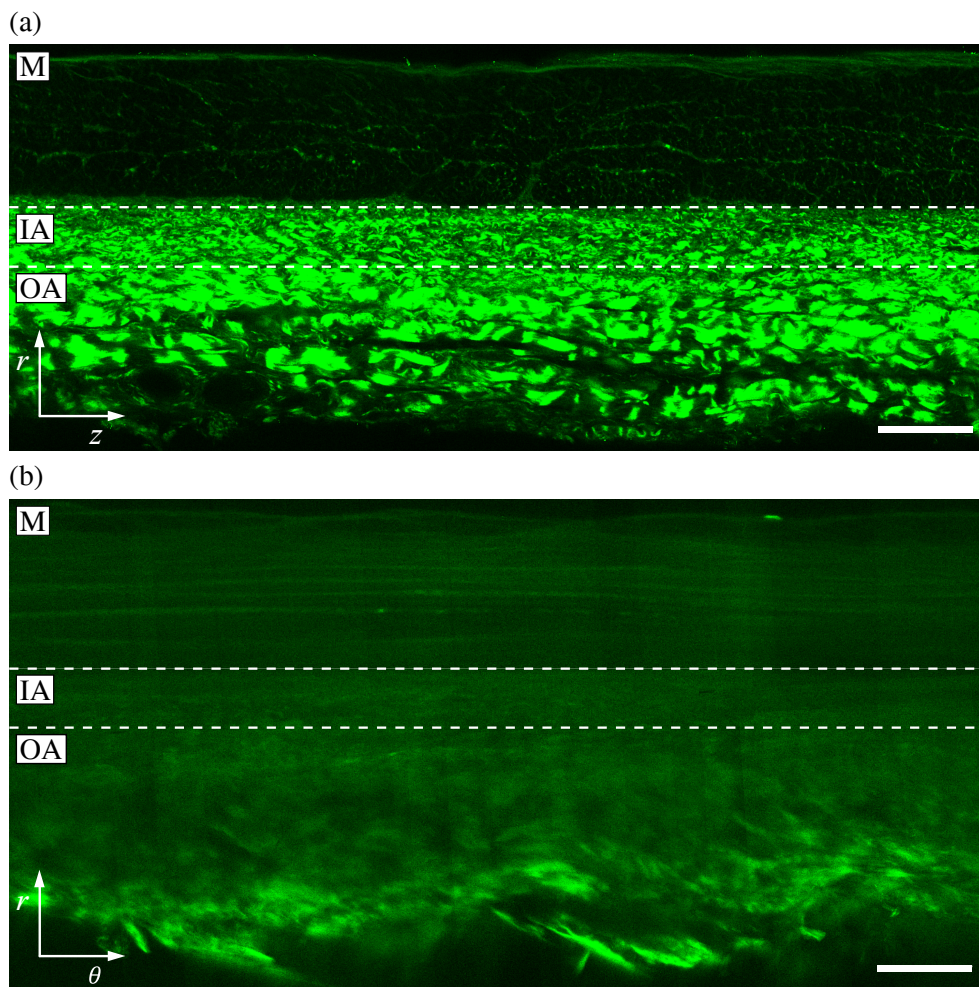
Figure 3.26   Out-of-plane scan of the sample N with the layers media (M), the inner (IA)
               and outer adventitia (OA): (a) out-of-plane scan in the longitudinal direction;
               (b) out-of-plane scan in the circumferential direction. Scale bar, 200 µm.

Figure 3.27 shows the out-of-plane scan of sample LI, with the intima on the upper side of the sample. The stamp was indented with the force of $1\,\text{N}$ in the longitudinal direction, so the circumferential direction is shown on the horizontal axis. In the media (M) and the inner adventitia (IA) a strong SHG signal of the straight collagen fibers is recorded. The fibers are oriented in the circumferential direction. In the outer adventitia (OA) the collagen fiber bundles show the typical wavy structure. The thickness of the whole sample is gradually decreasing over the lesion. Close to the lesion all the fibers are nearly straightened out due to the supra-physiological load acting on the sample. Under the stamp the whole sample is compressed evenly, and the media nearly kept its thickness. The sides next to the lesion are rising on a flat angle, as presented in Figure 3.16.

Figure 3.27   Out-of-plane scan of the sample LI with the lesion at the lower right side of the image and the visible layers media (M), the inner (IA) and outer adventitia (OA). Scale bar, $200\,\mu\text{m}$.

In Figure 3.28 the out-of-plane SHG scan of sample LII is shown, with the intima starting at the top. The stamp was indented with the force of $2\,\mathrm{N}$ in the longitudinal direction, so the circumferential direction is shown on the horizontal axis. SHG signal is recorded in the media and the inner adventitia shows collagen fibers oriented in the circumferential direction. In the outer adventitia the fibers become thicker until they appear as thick fiber bundles. Close to the lesion, all the fibers trough the thickness of the sample are straightened out. The media and the adventitia are getting gradually thinner over the entire lesion. As presented in Figure 3.17, the flanks are rising with a flat angle from the lesion, when the stamp is indenting in the longitudinal direction.

Figure 3.28   Out-of-plane scan of the sample LII with the lesion at the lower right side of the image and the visible layers media (M), the inner (IA) and outer adventitia (OA). Scale bar, $200\,\mu\mathrm{m}$.

Figure 3.29 shows the out-of-plane SHG scan of sample CI, with the intima starting from the top. The stamp was indented with the force of $1\,N$ in the circumferential direction, so the longitudinal direction is shown on the horizontal axis. The collagen fibers in the media are oriented in the circumferential direction and therefore, no SHG signal could be recorded. In the inner adventitia, the SHG signal becomes stronger when the fibers fulfill the orientation change, as described in Figure 3.24. The outer adventitia shows the typical wavy collagen fiber bundle structure in some parts, but most of the fibers are straightened out and no wavy structure is detected, especially in parts close to the lesion. Getting closer to the lesion the media and the adventitia become thinner. The scan shows that the media is compressed heavily and in the adventitia no gap is detected between the fibers.
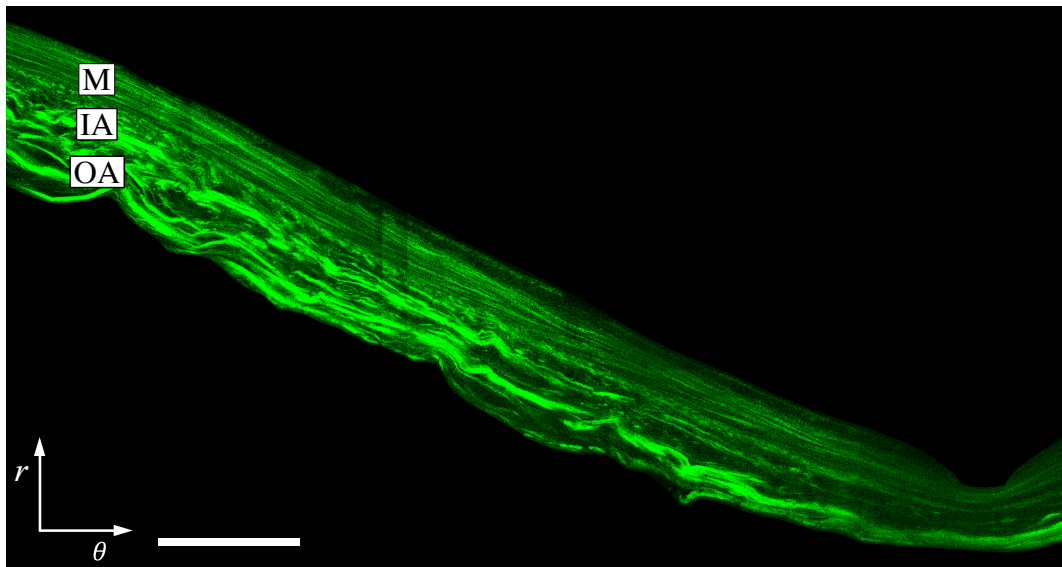

Figure 3.29   Out-of-plane scan of the sample CI with the lesion at the lower right side of the image and the visible layers media (M), the inner (IA) and outer adventitia (OA). Scale bar, $200\,\mu m$.

In Figure 3.30 the out-of-plane SHG scan of sample CII is shown, with the intima starting at the top. The stamp was indented with the force of $2\,\mathrm{N}$ in the circumferential direction, so the longitudinal direction is shown on the horizontal axis. In the main part of the media (M) no fibers are visible, because the fibers are aligned in the circumferential direction. In the inner adventitia (IA) some fibers are visible. The fibers are primarily oriented in the circumferential direction but closer to the outer adventitia (OA) the fibers fulfill a change in orientation towards the longitudinal direction. The thick collagen fiber bundles in the outer adventitia show still the typical wavy structure and are straightened out close to the lesion. This occurs due to the supra-physiological load which was applied by the stamp indentation. This out-of-plane SHG scan shows that the whole sample is deformed heavily. The thickness of the sample becomes gradually thinner over the entire lesion. The fibers in the media are pushed aside, so the media is compressed severely. The fibers in the adventitia are compressed and no gap between the single fiber bundles is visible.
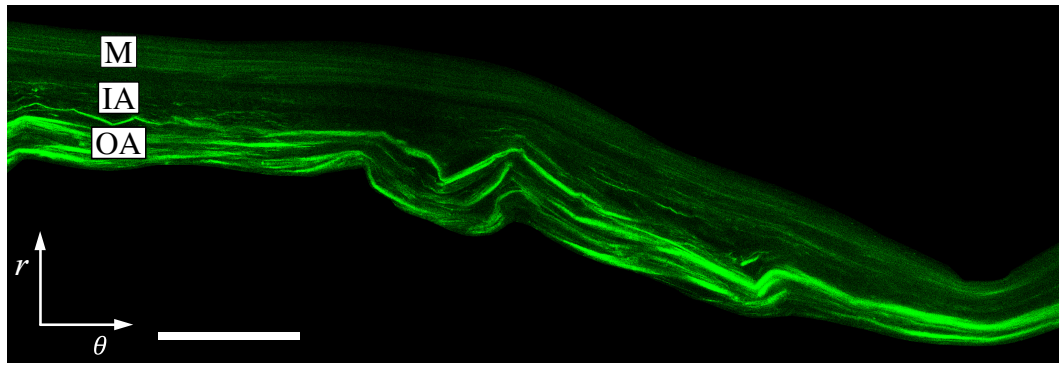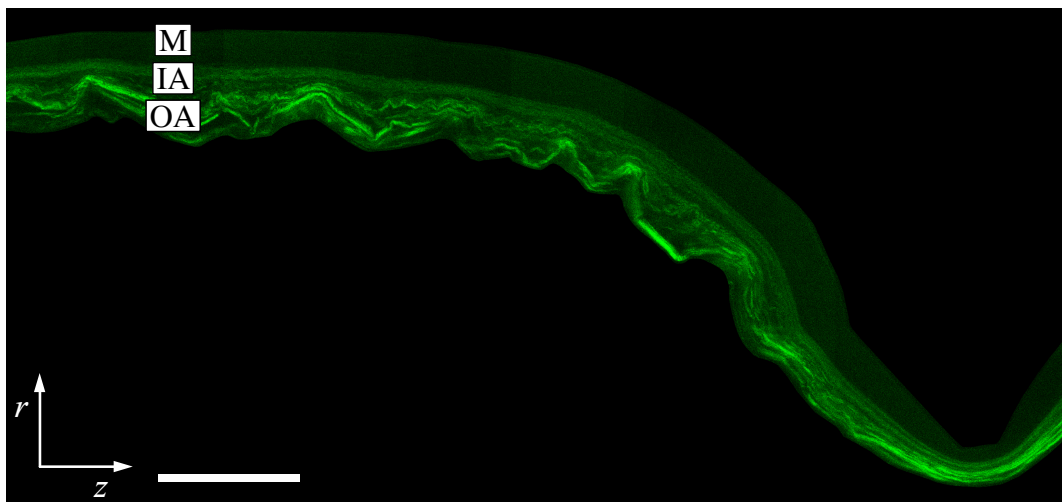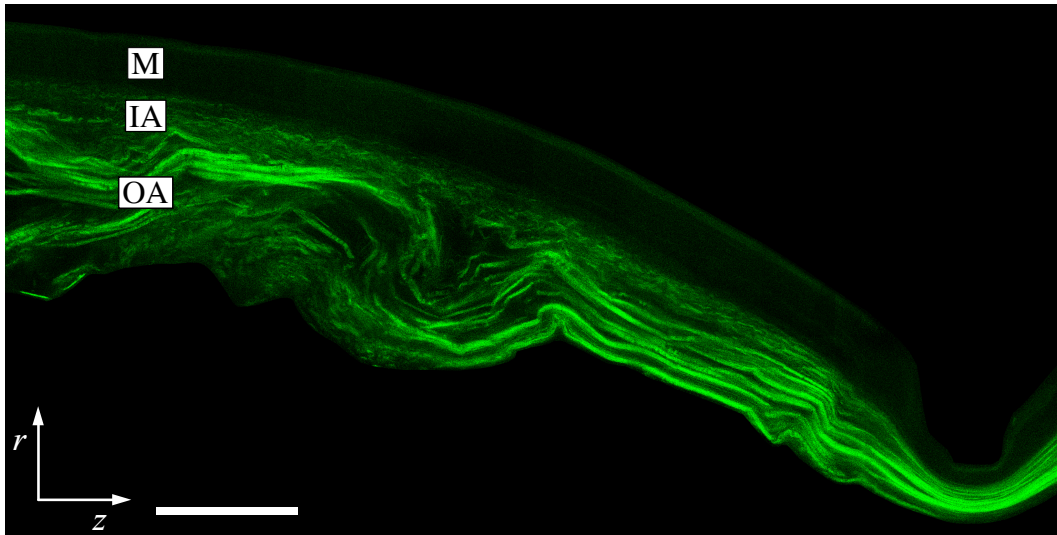

Figure 3.30   Out-of-plane scan of the sample CII with the lesion at the lower right side of the image and the visible layers media (M), the inner (IA) and outer adventitia (OA). Scale bar, $200\,\mu\mathrm{m}$.

The structural parameters α, κ_{ip} and κ_{op} of the tested samples were determined from the in-plane and out-of-plane SHG images. In Table 3.1, the results of the microstructural analysis are listed. For the whole adventitia, only one set of structural parameters was determined. In the samples LI and LII, in which the stamp indented in the longitudinal direction at the angle $\iota = 0°$, in the sample the mean fiber angle α becomes bigger when the indentation force increases. In comparison, in the samples CI and CII, in which the stamp indented in circumferential direction at the angle $\iota = 90°$, α decreases with greater indentation force. This mechanism occurs exactly the other way around in the adventitia. The in-plane dispersion quantified by κ_{ip} was found to be smaller in the media than in the

adventitia, which is consistent with the findings for human aortas by Niestrawska et al. [21]. However, κ_{ip} increases in the media if the stamp indents with a greater indentation force. In the adventitia, this mechanism seems to operate the other way around and κ_{ip} is decreasing. This counts for both tested stamp orientations. For the out-of-plane dispersion quantity κ_{op}, no trend can be observed.

Table 3.1   Structural parameters α, κ_{ip}, κ_{op} for the media (M) and the adventitia (A) of the native sample (N) and the indented samples (LI,LII, CI and CII) obtained from SHG images. ι is the stamp indentation angle. F_{ind} indicates the indentation force the sample was tested with. T_0 defines the thickness of the sample before the test and t indicates the thickness of the sample at the specific location at the distance k from the center of the sample. λ_r defines the compression between the untested thickness and the specific location in the sample.

Sample	ι [°]	F_{ind} (p_{ind}) [N] ([MPa])	Location	$k_{\max}$ [mm]	T_0 [μm]	t [μm]	λ_r [-]	Layer	α [°]	κ_{ip} [-]	κ_{op} [-]
N	-	-	Native	-	820	520	0.63	M	6	0.071	0.46
								A	56	0.172	
LI	0	1 (4.15)	Virgin	1.25	845	305	0.36	M	6	0.033	0.47
								A	49	0.130	
			Damaged			160	0.19	M	9	0.071	0.48
								A	39	0.570	
LII	0	2 (8.3)	Virgin	1.0	973	200	0.20	M	14	0.104	0.49
								A	55	0.245	
			Damaged			150	0.15	M	27	0.156	0.48
								A	42	0.169	
CI	90	1 (4.15)	Virgin	0.65	663	220	0.33	M	2	0.027	0.47
								A	63	0.123	
			Damaged			190	0.28	M	1	0.020	0.40
								A	65	0.117	
CII	90	2 (8.3)	Virgin	0.6	938	380	0.41	M	3	0.103	0.40
								A	69	0.151	
			Damaged			185	0.20	M	2	0.163	0.48
								A	56	0.148	

4 Discussion

The goal of this master thesis was to deepen the knowledge of the morphology of porcine RCA. Furthermore, new *in vitro* experimental methods, combined with an advanced strategy for the application of established imaging techniques were used, for the purpose of quantifying stent-triggered mechanical and morphological changes in porcine RCA due to CSI. The *in vivo* loading scenario during CSI in an *in vitro* environment could be simulated with the experimental testing device LAESIO. Tissue samples from porcine RCA were stretched biaxially with an assumed physiological loading and indented with a stamp in the shape of a straight stent-strut. To analyze and quantify the mechanical changes, the mechanical response was measured before and after the indentation. Subsequently, the morphological investigation of structural changes was realized with 3D-surface and SHG scans. The observed mechanical behavior of porcine RCA under physiological load can be described as a soft viscoelastic tissue with a small hysteresis, confirming the typical characteristics of coronary arteries. The tissue wall consists of three layers: the intima, media and adventitia. The intima was not detectable, because for young individuals this layer is almost none existing [5]. The media contains a fine collagen structure and is more likely to be oriented in the circumferential direction. The adventitia can be subdivided into two parts: the inner adventitia with thicker fibers, which have a high tendency to align in the longitudinal direction and the outer adventitia with wavy fiber bundles, which tend to align towards the circumferential direction. In this study, these layers were investigated and compared with reference to the severity of damage due to CSI. Several reasons for tissue damage mechanisms could be identified: (i) the stamp orientation, i.e. the indentation angle, (ii) the used indentation force and (iii) the distance between a specific point of interest and the center of the lesion.

Mechanical damage, due to supra-physiological loading, occurring when the stamp is indented, is defined as softening of the tissue. When the stamp orientation was parallel to the fiber orientation in the media, minor mechanical damage was observed, compared to a perpendicular stamp orientation. Consequently, when indenting the stamp in perpendicular orientation, more severe damage was monitored. These results point out that the stamp orientation is an important indicator to the degree of tissue softening.

Furthermore, the indentation force has an impact on the degree of softening, with the higher force of $2\,N$, softening the tissue more severe than the force of $1\,N$. This effect could be shown in all tested samples and in both, i.e. longitudinal and circumferential, directions. However, damage was higher for the longitudinal stamp orientation, compared to the circumferential orientation (see Section 3.3). The 3D-surface scans (Figures 3.16 - 3.19) show an illustration of the damaged sample geometry. For samples, where the stamp

indented in the longitudinal direction (Figures 3.16, 3.17), the flanks perpendicular to the stamp rise on a flat angle, because the stamp cannot push the fibers aside. The collagen fibers oriented in the circumferential direction of the media and the inner adventitia resist against the indentation and get straightened out. This is confirmed by the merged out-of-plane scans. For the samples, where the stamp indented in the circumferential direction, the flanks perpendicular to the stamp are rather steep, because the stamp is able to push through the fibers as long as the stamp orientation equals the orientation of the fibers. This triggers delamination of the layers, especially for the higher indentation force of $2\,\mathrm{N}$.

Third, the severity of damage depends on the distance between a specific point of interest and the center of the lesion. The distance k_{max} defines the distance between the virgin tissue and the center of the indentation. Results show that the extent of the lesion in the longitudinal and the circumferential direction shrink at a higher indentation force. The structural parameters α and κ_{ip} changed due to the indentation of the stamp. If the stamp was indented in the longitudinal direction, the degree of dispersion in the damaged tissue increased, shown by greater values for κ_{ip}. The mean fiber angle α in the media increased and in the adventitia it decreased, assuming that the fibers orient towards the stamp orientation. For the damaged tissue, where the stamp indented in the circumferential direction, the mean fiber angle α and the structural parameter κ_{ip} in the media, decreased. In the adventitia α increased, assuming that the fibers are pushed aside, the fiber density is increasing and the fibers have to align, resulting in a decreasing dispersion.

To diminish tissue damage due to CSI, the author suggests that the stent should be designed with struts in the longitudinal direction and the force should be small, because for a lower force the softening in the longitudinal and the circumferential direction is similar for both stamp indentation angles (see Figure 3.11). The longitudinal strut orientation is proposed, because the fibers in the media are oriented in the circumferential direction and during the experiments the stamp was not able to cause deep tissue damage. Schwartz et al. [13] documented that a severe penetration of the tissue leads to neointima hypoplasia.

The aim of this thesis was to test CA and to gain basic knowledge about CSI injuries from a biomechanical point of view. Nevertheless, this study was a feasibility study and had some limitations. First, the mechanical response of the connective tissue was neglected, because the tissue was tested without any support on the adventitia. Further, a constant pressure distribution under the stamp is assumed, because the tissue profile under the sample was homogeneous, but most likely there are stress singularities at both ends of the stamp. Another limitation is that the sample was assumed to be incompressible, because it was not possible to measure the actual thickness during the test and therefore, λ is assumed constant during the experiment. However, Table 3.1 shows that thickness of the sample changes during biaxial testing, which states compressibility of the tissue. The small amount of samples is another limitation and future studies should perform similar testing protocols with a bigger sample size. Because of the insights gained in morphological structure of porcine RCA, future studies need to test various stamps, differing in length, orientation and structure, to create an environment, which exhibits more similarities to a real, implanted stent. Further, different stamp forces should be used.

At this stage, it is difficult to formulate recommendations for the improvement of material models for FEA of CSI, which can help to simulate the presented damage mechanism. For continuum mechanical modeling, e.g., an expansion of the model of Holzapfel et al. [22], the implementation of an additional parameter set, which allows to fit the model to an experimentally derived function describing the stress-stretch relationship in dependency of the compression, would be a feasible step.

5 Conclusion

This master thesis and the included feasibility study tested new *in vitro* experimental methods with the experimental testing device LAESIO [2], combined with an advanced strategy for the application of established imaging techniques, to quantify stent-triggered mechanical and morphological changes in porcine CA. Porcine RCA tissue samples were biaxially stretched with an assumed physiological loading, and a stamp in the shape of a straight stent-strut was indented. The mechanical response was measured before and after the indentation to determine the softening of the tissue, due to supra-physiological loading. Afterwards, the structural changes were investigated with 3D-surface and SHG scans. Finally, the experimental and imaging data were analyzed and damage mechanisms were identified.

The tissue of the tested porcine RCA can be described as soft viscoelastic material comprising three layers, the intima, media and adventitia. The media contains fine concentric collagen fibers with small dispersion. The adventitia can be subdivided into the inner and outer adventitia. In the inner adventitia thicker fibers tend to align in the circumferential direction, while the wavy fiber bundles of the outer adventitia point mostly towards the longitudinal direction. The dispersion in the adventitia is significantly higher than in the media. An increase of the indentation force led to more softening in the longitudinal and in the circumferential direction in all tested specimens. However, the percentage gain in the stretch, due to the softening was higher for all tests in the circumferential direction. This effect was more severe when the stamp indented in the longitudinal direction.

The microstructural analysis showed that the characteristics of porcine RCA get influenced by certain damage mechanisms, when a stent-strut-like structure indents into the tissue. The severity of these damage mechanism depends significantly on the contact force between the coronary artery and the indenting stent-strut, the stamp orientation, and the location, i.e. the distance between the point of interest inside the tissue and the center of the stamp indentation.

Finally, the results of this master thesis will help to establish urgently needed basic knowledge about CSI injuries from a biomechanical point of view. To reach more precise information more samples should be tested and microstructure should be investigated more intensly, to achieve the final goal: a verified mathematical material damage model.

Bibliography

[1] Mühlberger V, Kaltenbach L, Bates K, Ulmer H. Cardiac catheterization coronary angiography (CA) and percutaneous coronary interventions (PCI) in Austria during the year 2018. Austrian J. of Cardiology 2020;27(1–2):32–35.

[2] Geith MA, Sommer G, Schratzenstaller T, Holzapfel GA. Biomechanical and structural quantification of vascular damage: A unique investigation of stent implantation. Artery Research 2017;20(0):50. doi:10.1016/j.artres.2017.10.025

[3] Schünke M, Schulte E, Schumacher U, Voll M, Wesker KH. PROMETHEUS Innere Organe LernAtlas der Anatomie, vol. 5. Thieme 2018. ISBN 978–3–13–139532–0. doi:10.1055/b–006–149645

[4] Fanghänel J, Waldeyer A. Waldeyer Anatomie des Menschen. De Gruyter 2003. doi:10.1515/9783110228632

[5] Holzapfel GA, Gasser TC, Ogden RW. A new constitutive framework for arterial wall mechanics and a comparative study of material models. J. Elast. 2000;61(1/3):1–48. doi:10.1023/A:1010835316564

[6] Holzapfel GA. Collagen in arterial walls: biomechanical aspects. In Collagen. Springer 2008;285–324

[7] Chen H, Kassab G. Microstructure–based biomechanics of coronary arteries in health and disease. J. Biomech. 2016;49(12):2548–59. doi:10.1016/j.jbiomech.2016.03.023

[8] Stefanini GG, Holmes DR. Drug–eluting coronary–artery stents. N. Engl. J. Med. 2013;368(3):254–265. doi:10.1056/nejmra1210816

[9] Serruys PW, de Jaegere P, Kiemeneij F, Macaya C, Rutsch W, Heyndrickx G, et al.. A comparison of balloon–expandable–stent implantation with balloon angioplasty in patients with coronary artery disease. N. Engl. J. Med. 1994;331(8):489–495. doi: 10.1056/NEJM199408253310801

[10] Kiousis DE, Wulff A, Holzapfel GA. Experimental studies and numerical analysis of the inflation and interaction of vascular balloon catheter–stent systems. Ann. Biomed. Eng. 2009;27(2):315–330. doi:10.1007/s10439–008–9606–9

[11] Serruys PW, Unger F, Sousa JE, Jatene A, Bonnier HJ, Schönberger JP, et al.. Comparison of coronary–artery bypass surgery and stenting for the treatment of multivessel disease.   N. Engl. J. Med. 2001;344(15):1117–1124.   doi: 10.1056/NEJM200104123441502

[12] Bønaa KH, Mannsverk J, Wiseth R, Aaberge L, Myreng Y, Nygård O, et al.. Drug–eluting or bare–metal stents for coronary artery disease. N. Engl. J. Med. 2016; 375(13):1242–1252. doi:10.1056/nejmoa1607991

[13] Schwartz RS, Huber KC, Murphy JG, Edwards WD, Camrud AR, Vlietstra RE, et al.. Restenosis and the proportional neointimal response to coronary artery injury: Results in a porcine model. J. Am. Coll. Cardiol. 1992;19(2):267–274. doi: 10.1016/0735–1097(92)90476–4

[14] Schwartz RS, Murphy JG, Edwards WD, Camrud AR, Vliestra RE, Holmes DR. Restenosis after and balloon angioplasty and a practical and proliferative model and in porcine and coronary arteries.   Circulation 1990;82(6):2190–2200.   doi: 10.1161/01.CIR.82.6.2190

[15] Sommer G, Eder M, Kovacs L, Pathak H, Bonitz L, Mueller C, et al.. Multiaxial mechanical properties and constitutive modeling of human adipose tissue: A basis for preoperative simulations in plastic and reconstructive surgery. Acta Biomater. 2013;9(11):9036–9048. doi:10.1016/j.actbio.2013.06.011

[16] Sommer G, Haspinger DC, Andrä M, Sacherer M, Viertler C, Regitnig P, et al.. Quantification of shear deformations and corresponding stresses in the biaxially tested human myocardium. Ann. Biomed. Eng. 2015;43(10):2234–2348. doi: 10.1007/s10439–015–1281–z

[17] Millard AC, Campagnola PJ, Mohler W, Lewis A, Loew LM. Second harmonic imaging microscopy. In Biophotonics, Part B, vol. 361 of Methods in Enzymology. Academic Press 2003;47–69. doi:10.1016/S0076–6879(03)61005–0

[18] Stockert J, Blazquez-Castro A. Fluorescence Microscopy in Life Sciences. Bentham Science Publishers 2017

[19] Freund I, Deutsch M, Sprecher A. Connective tissue polarity. Optical second–harmonic microscopy, crossed–beam summation, and small–angle scattering in rat–tail tendon. Biophys. J. 1986;50(4):693–712. doi:10.1016/S0006–3495(86)83510–X

[20] Denk W, Strickler J, Webb W. Two–photon laser scanning fluorescence microscopy. Science 1990;248(4951):73–76. doi:10.1126/science.2321027

[21] Niestrawska JA, Regitnig P, Viertler C, Cohnert TU, Holzapfel GA. Mechanics and microstructure of healthy human aortas and AAA tissues: experimental analysis and modeling. J. R. Soc. Interface 2016;13(124). doi:10.1098/rsif.2016.0620

[22] Holzapfel GA, Niestrawska JA, Ogden RW, Reinisch AJ, Schriefl AJ. Modelling non–symmetric collagen fibre dispersion in arterial walls. J. R. Soc. Interface 2015; 12(106):20150188. doi:10.1098/rsif.2015.0188

[23] Čepin U. 2019. Chemical fixation for structural analyses of arterial tissue . Bachelor's Thesis, Graz University of Technology, Institute of Biomechanics

[24] Pitt KE, Campbell LD, Skubitz AP, Somiari SB, Sexton KC, Pugh RS. Collection, storage, retrieval and distribution of biological materials for research. Cell Preserv. Technol. 2008;6(1):3–58. doi:10.1089/cpt.2008.9997

[25] Heiml MS. 2019. Mechanical response of arteries to stenting . Bachelor's Thesis, Graz University of Technology, Institute of Biomechanics

[26] Katz G, Harchandani B, Shah B. Drug–eluting stents: the past, present, and future. Curr. Atheroscler. Rep. 2015;17(3):11. doi:10.1007/s11883–014–0485–2

[27] van Andel CJ, Pistecky PV, Borst C. Mechanical properties of porcine and human arteries: implications for coronary anastomotic connectors. Ann. Thorac. Surg. 2003; 76(1):58–64. doi:10.1016/S0003–4975(03)00263–7

[28] Eilaghi A, Flanagan JG, Brodland GW, Ethier CR. Strain uniformity in biaxial specimens is highly sensitive to attachment details. J. Biomech. Eng. 2009;131(9). doi: 10.1115/1.3148467

[29] Schriefl AJ, Wolinski H, Regitnig P, Kohlwein SD, Holzapfel GA. An automated approach for three–dimensional quantification of fibrillar structures in optically cleared soft biological tissues. J. R. Soc. Interface 2013;10(80):20120760. doi: 10.1098/rsif.2012.0760

[30] Zehentner F. 2018. Transfer of sourcecode to Java for implementation of angular dispersion analysis plug–in into ImageJ . Master's Thesis, Graz University of Technology, Institute of Biomechanics